

Article

Novel Laser-Assisted Chemical Bath Synthesis of Pure and Silver-Doped Zinc Oxide Nanoparticles with Improved Antimicrobial and Photocatalytic Properties

Samer H. Zyoud^{1,2,3,4,*}, Samer O. Alalalmeh^{3,5}, Omar E. Hegazi^{3,5}, Ibrahim S. Yahia^{6,7,8}, Heba Y. Zahran^{6,7,8}, Hamed Abu Sara^{3,5}, Samir Haj Bloukh^{3,5}, Moyad Shahwan^{3,5}, Ahed H. Zyoud⁹, Nageeb Hassan^{3,5}, Akram Ashames^{3,5}, Malek G. Daher¹⁰, Ghaseb N. Makhadmeh¹¹, Ammar Jairoun^{12,13}, Naser Qamhieh¹⁴ and Mohamed Sh. Abdel-wahab¹⁵

- ¹ Department of Mathematics and Sciences, Ajman University, Ajman P.O. Box 346, United Arab Emirates
 - ² Nonlinear Dynamics Research Center (NDRC), Ajman University, Ajman P.O. Box 346, United Arab Emirates
 - ³ Center of Medical and Bio-Allied Health Sciences Research, Ajman University, Ajman P.O. Box 346, United Arab Emirates
 - ⁴ School of Physics, Universiti Sains Malaysia (USM), Minden 11800, Malaysia
 - ⁵ Department of Clinical Sciences, College of Pharmacy and Health Sciences, Ajman University, Ajman P.O. Box 346, United Arab Emirates
 - ⁶ Laboratory of Nano-Smart Materials for Science and Technology (LNSMST), Research Center for Advanced Materials Science (RCAMS), King Khalid University, P.O. Box 9004, Abha 61413, Saudi Arabia
 - ⁷ Research Center for Advanced Materials Science (RCAMS), King Khalid University, P.O. Box 9004, Abha 61413, Saudi Arabia
 - ⁸ Nanoscience Laboratory for Environmental and Biomedical Applications (NLEBA), Metallurgical Lab.1., Department of Physics, Faculty of Education, Ain Shams University, Roxy, Cairo 11757, Egypt
 - ⁹ Department of Chemistry, SSERL, An-Najah National University, Nablus P.O. Box 7, Palestine
 - ¹⁰ Physics Department, Islamic University of Gaza, Gaza P.O. Box 108, Palestine
 - ¹¹ Department of Physics, Bio-Medical Physics Laboratory, Jordan University of Science and Technology, Irbid P.O. Box 3030, Jordan
 - ¹² School of Pharmaceutical Sciences, Universiti Sains Malaysia (USM), Gelugor 11500, Malaysia
 - ¹³ Health and Safety Department, Dubai Municipality, Dubai P.O. Box 67, United Arab Emirates
 - ¹⁴ Department of Physics, United Arab Emirates University, Al-Ain P.O. Box 15551, United Arab Emirates
 - ¹⁵ Materials Science and Nanotechnology Department, Faculty of Postgraduate Studies for Advanced Sciences, Beni-Suef University, Beni-Suef 62511, Egypt
- * Correspondence: s.zyoud@ajman.ac.ae



Citation: Zyoud, S.H.; Alalalmeh, S.O.; Hegazi, O.E.; Yahia, I.S.; Zahran, H.Y.; Sara, H.A.; Bloukh, S.H.; Shahwan, M.; Zyoud, A.H.; Hassan, N.; et al. Novel Laser-Assisted Chemical Bath Synthesis of Pure and Silver-Doped Zinc Oxide Nanoparticles with Improved Antimicrobial and Photocatalytic Properties. *Catalysts* **2023**, *13*, 900. <https://doi.org/10.3390/catal13050900>

Academic Editors: Kangqiang Lu and Weiya Huang

Received: 2 April 2023
Revised: 3 May 2023
Accepted: 15 May 2023
Published: 17 May 2023



Copyright: © 2023 by the authors. Licensee MDPI, Basel, Switzerland. This article is an open access article distributed under the terms and conditions of the Creative Commons Attribution (CC BY) license (<https://creativecommons.org/licenses/by/4.0/>).

Abstract: Antimicrobial resistance poses a significant threat to global health, amplified by factors such as water scarcity and suboptimal hygienic practices. Addressing AMR effectively necessitates a comprehensive strategy encompassing enhanced access to potable water, developing innovative antibiotics, and exploring alternative treatment modalities, such as harnessing solar photocatalysis with zinc oxide nanoparticles for water purification and antimicrobial applications. The Laser-Assisted Chemical Bath Synthesis (LACBS) technique facilitates the fabrication of pure ZnO nanostructures, providing a potentially efficacious solution for mitigating pathogen proliferation and managing wastewater. The photocatalytic degradation of MB and MO dyes was investigated using blue laser light at 445 nm, and degradation rates were determined accordingly. Ag-doped ZnO nanostructures were characterized through X-ray diffraction, field emission scanning electron microscopy, energy dispersive X-ray spectroscopy, and Fourier-transform infrared spectroscopy. The antimicrobial efficacy of LACBS-synthesized ZnO nanoparticles was assessed against *C. albicans*, *S. aureus*, *B. subtilis*, *E. coli*, and *K. pneumoniae* using the disc diffusion method, revealing 40 mm, 37 mm, 21 mm, 27 mm, and 45 mm inhibition zones at the highest concentration of doped-Ag (4.5%), respectively. These inhibition zones were measured in accordance with the guidelines established by the Clinical and Laboratory Standards Institute. X-ray diffraction patterns for ZnO, ZnOAg(1.5%), ZnO:Ag(3%), and ZnO:Ag(4.5%) samples revealed variations in intensity and crystallinity. Scanning electron microscopy exposed morphological disparities among the nanostructures, while energy-dispersive X-ray spectroscopy verified their elemental compositions. UV-Vis absorption analyses inspected the optical band gaps, and Fourier-transform infrared spectra identified the stretching mode of metal-oxygen

bonds. Under blue laser irradiation, Ag-doped ZnO exhibited enhanced photocatalytic activity during the photocatalytic degradation. These nanoparticles, synthesized via the cost-effective and straightforward LACBS method, benefit from silver doping that augments their electron-trapping properties and photocatalytic activity, thereby enabling efficient dye degradation. Consequently, Ag-doped ZnO nanoparticles hold promise as a potent solution for counteracting drug-resistant microorganisms and as an effective disinfectant.

Keywords: ZnO nanoparticles; Ag-doping; photocatalysis; antimicrobial activity; LACBS; antimicrobial resistance (AMR); zone of inhibition

1. Introduction

Antimicrobial resistance (AMR) is a complex global health threat with severe implications for medicine, humanity's survival, and the environment [1–3]. Leading causes include the overuse and misuse of antimicrobial agents, their use in agriculture and animal husbandry, poor hygiene practices, natural evolution, and genetic phenomena [3–9]. AMR increases morbidity, mortality, healthcare costs, and economic losses [1–3,10], with an estimated annual cost of \$55 billion in the United States alone and a potential global cost exceeding a trillion dollars [11–13]. Moreover, AMR is responsible for over a million deaths annually, which could rise to 10 million within three decades if adequate measures are not implemented [2,14,15]. Numerous pathogens contribute to resistance-related deaths, while other microorganisms, such as *Candida albicans*, *Clostridium difficile*, and *Bacillus subtilis*, also demonstrate AMR [2,10,14,16–19]. Water scarcity, exacerbated by population growth and economic demand, worsens AMR's impact on flora and fauna [4,5]. Alternative water sources like wastewater reuse and advanced oxidation processes can address water scarcity and persistent organic pollutants, which pose a significant challenge to traditional water treatment efforts [20–23]. Therefore, implementing strategies to prevent and control the spread of AMR critical [13,24,25].

Addressing the complex interplay between the lack of clean water and AMR demands a comprehensive approach rather than relying solely on reducing human antimicrobial usage. The solution should encompass improving access to safe water, implementing effective water treatment processes, improving antibiotic stewardship and public health literacy, reducing antibiotic use in agriculture and animal husbandry, and promoting the development of new antibiotics and alternative therapies [1,14,15,26–29]. Several inventive techniques like solar photocatalysis and nanoparticle drug development have shown potential in addressing the lack of access to clean water and AMR [29,30]. Among these approaches, utilizing zinc oxide (ZnO) nanoparticles as antimicrobial agents and solar photocatalysts are promising avenues [31].

Various studies have revealed that solar photocatalysis is a promising method for eliminating organic pollutants and increasing water purity. ZnO, a versatile semiconductor, is an attractive material for photocatalytic water treatment due to its excellent thermal, mechanical, and optoelectronic properties [32,33]. ZnO can be synthesized in diverse morphologies, such as nanorods, nanoparticles, and thin films. Doping ZnO with metallic materials, such as silver, magnesium, or aluminum, can enhance its efficiency and tune its performance within specific wavelength ranges [34]. These metallic dopants create new energy levels in ZnO, effectively suppressing the recombination of charge carriers and thus improving its photocatalytic activity [35].

Additionally, numerous studies have substantiated the potent antimicrobial activity of Zinc oxide nanoparticles against a broad spectrum of pathogens [36–41]. These nanoparticles exhibit both bactericidal and bacteriostatic properties, which are thought to be mediated by various mechanisms that arise from ZnO's unique physicochemical characteristics [42]. These mechanisms include the generation of reactive oxygen species (ROS), the release of zinc ions (Zn^{2+}), and the attachment and accumulation of nanoparticles

on the target organism's cell wall and inside the cell [37,40,43]. The stated actions have the potential to lead to the eradication of targeted pathogens. Moreover, integrating dopants can significantly amplify the antimicrobial effectiveness of Zinc oxide nanoparticles. For instance, silver can impede cell membrane and DNA replication, copper can trigger protein inactivation, and nickel can exhibit similar bacteriostatic properties when utilized [30].

Laser-assisted systems operating in continuous wave and pulsed modes, encompassing the ultraviolet to infrared range, have exhibited significant potential for treating, designing, and fabricating functional nanomaterials [44]. This rapidly evolving field offers straightforward, economical, and scalable methodologies coupled with high-yield production capabilities [45]. Laser-Assisted Chemical Bath Synthesis (LACBS) technology, by exerting precise control over chemical reactions, thermal effects, and nucleation and particle growth phenomena during nanostructure synthesis, can generate nanostructures possessing desirable characteristics such as larger surface area nanoparticles for the production of antimicrobial agents [36,45].

LACBS is a wet chemical synthesis process that employs laser irradiation to promote the controlled precipitation of zinc oxide (ZnO) nanostructures. This method differs from laser ablation, a purely physical procedure involving material removal from a solid surface using a focused laser beam. By combining the merits of both chemical bath synthesis and laser irradiation, LACBS enhances the control over the resulting nanostructures' size, morphology, and crystallinity. This technique is based on the photothermal effect produced by a focused laser, which generates a localized temperature field with exceptional control [46]. Consequently, this allows for meticulous manipulation of fabrication parameters and physical properties, thereby improving nanostructure characteristics [47]. ZnO nanostructures are cultivated via LACBS, utilizing chemical bath synthesis and laser irradiation. Zinc salts and complexing agents are dissolved to create a chemical bath, while laser irradiation augments the nucleation process, forming homogeneous ZnO nuclei that develop into larger structures. In addition to laser irradiation parameters, factors such as concentration, temperature, pH, and reaction time modulate the nanostructure's morphology, size, and orientation [29,46].

In recent years, there has been a surge in the scientific community's interest in zinc oxide, particularly in its antimicrobial and solar photocatalytic properties. This has been demonstrated through numerous studies, which have also explored the potential of silver-doped ZnO [31,41,48–52]. Despite the promising potential of zinc oxide, previous research has not examined the use of LACBS in producing undoped and Ag-doped ZnO materials. The LACBS technique has demonstrated exceptional promise in creating ZnO-based materials with extraordinary antimicrobial properties in this work. This study aims to investigate the efficacy of pure and Ag-doped ZnO nanostructures synthesized via LACBS as potent antimicrobial and photocatalytic agents, contributing to developing efficient and sustainable solutions for pathogen control and wastewater treatment.

2. Results and Discussion

2.1. X-ray Diffraction (XRD)

Figure 1 illustrates the X-ray diffraction (XRD) patterns for a series of samples, including pure ZnO, ZnO:Ag_(1.5%), ZnO:Ag_(3%), and ZnO:Ag_(4.5%). The XRD pattern for the pure ZnO sample reveals distinct peaks corresponding to multiple lattice planes, thereby verifying the hexagonal wurtzite crystal structure and suggesting the presence of a single-phase crystalline material with preferential growth of nanostructures along the b-axis. Conversely, the XRD patterns for the ZnO:Ag samples exhibit well-defined yet narrower peaks, indicating good crystallinity with diminished intensity for characteristic ZnO peaks, implying a reduction in ZnO crystallinity. The absence of silver oxide peaks and the improbability of Ag⁺ ions substituting Zn²⁺ ions in the ZnO lattice—due to the significant difference in ionic radii—suggest the formation of a crystalline Ag phase and the persistence of Ag agglomerates on the ZnO surface. An analysis of the XRD patterns for specific ZnO-Ag samples demonstrates that the highest intensity peak for ZnO-Ag_(1.5%), ZnO:Ag_(3%),

and ZnO:Ag_(4.5%) is located at the (101) lattice plane, indicating a preferential growth of nanostructures along the b-axis as well.

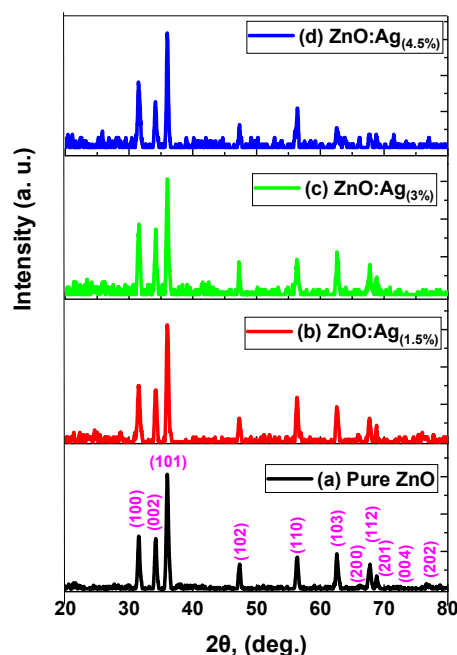


Figure 1. XRD spectra of samples (a) Pure ZnO, (b) ZnO:Ag_(1.5%), (c) ZnO:Ag_(3%), (d) ZnO:Ag_(4.5%).

Table 1 provides a comprehensive overview of the structural parameters for undoped and doped ZnO nanostructures generated through the LACBS method at various doping concentrations. These parameters encompass peak position (2θ), intensity, full width at half maximum (FWHM), lattice constants (a , b , and c), and internal strain stress (ϵ_a , ϵ_c) along the diffraction peak (101). These parameters remain predominantly consistent as doping concentration increases, although higher doping concentrations correspond with diminished diffraction intensity. The strain observed in these materials arises from a combination of intrinsic and extrinsic stresses, with the latter originating from defects and impurities.

Table 1. Lattice parameters and structure properties of pure and Ag-doped ZnO nanostructures of the highest diffraction peak (101).

	(h, k, l)	2θ , (deg)	d	β , (deg)	D , (Å)	$a=b$, (Å)	c , (Å)	$\frac{c}{a}$	ϵ_a	ϵ_c
Pure ZnO	101	36.16	2.47	0.78	1.87	2.87	4.97	1.73	−11.75	−4.56
ZnO:Ag _(1.5%)	101	36.19	2.49	0.79	1.85	2.87	4.96	1.73	−11.82	−4.63
ZnO:Ag _(3%)	101	36.20	2.49	0.86	1.70	2.86	4.96	1.73	−11.85	−4.66
ZnO:Ag _(4.5%)	101	36.87	2.51	0.88	1.66	2.81	4.87	1.73	−13.39	−6.33

Employing Bragg's equation and the Debye-Scherrer formula, researchers estimated the residual stress in undoped and doped ZnO nanostructures and computed the average crystallite size. An increase in the growth periods of hexamethylenetetramine (HMTA) may yield more significant grain expansion and decomposition of HMTA to OH^- , thereby creating more opportunities for Zn^+ and OH^- ions to recombine and augment the crystalline size of ZnO [33,53].

$$n\lambda = 2d\sin\theta \quad (1)$$

$$D(\text{Å}) = \frac{k\lambda}{\beta\cos\theta} \quad (2)$$

Utilizing Equations (3) and (4), relating to the diffraction angle (θ) and X-ray source wavelength (λ), the lattice constants (a , b , and c) of both doped and undoped ZnO were ascertained. The lattice parameters (a and c) listed in Table 1 closely align with those documented in the Joint Committee on Powder Diffraction Standards (JCPDS) card for ZnO. To calculate the perpendicular strain (ε_a) of doped and undoped ZnO nanostructures along the a-axis and the strain (ε_c) along the c-axis, equations incorporating the differences between actual and standard lattice constants were employed in Equations (5) and (6). In these equations, a_0 and c_0 represent the standard lattice constants for unstrained ZnO thin films, which were obtained from X-ray diffraction pattern data ($a_0 = 3.2494 \text{ \AA}$, and $c_0 = 5.2038 \text{ \AA}$, respectively). The standard lattice constant for unstrained ZnO thin films appears in JCPDS card no. 01-079-0206. Moreover, the computed ZnO bond lengths presented in Table 1 concur with the literature value of 1.9767 \AA [33,54].

$$a(\text{\AA}) = b(\text{\AA}) = \frac{\lambda}{\sqrt{3}\sin\theta} \quad (3)$$

$$c(\text{\AA}) = \sqrt{3}a \quad (4)$$

$$\varepsilon_a = \frac{a - a_0}{a_0} \times 100\% \quad (5)$$

$$\varepsilon_c = \frac{c - c_0}{c_0} \times 100\% \quad (6)$$

2.2. Scanning Electron Microscope (SEM)

In this investigation, scanning electron microscopy (SEM) was utilized to systematically analyze the morphological characteristics and dimensions of nanostructures synthesized from four distinct samples: pure ZnO, ZnO:Ag_(1.5%), ZnO:Ag_(3%), and ZnO:Ag_(4.5%). The acquired SEM micrographs, captured at various magnifications, unveiled that the pure ZnO nanoparticles possessed a uniform hexagonal particle structure. The introduction of Ag doping in ZnO:Ag samples led to the formation of distinctive nanostructures, which markedly altered the ZnO morphology. The SEM images demonstrated that both pure ZnO and ZnO:Ag_(1.5%) featured an assembly of well-aligned, high-density ZnO nanorods. In comparison, ZnO:Ag_(3%) manifested as uniformly agglomerated nanorods that were sparsely interconnected. Conversely, ZnO:Ag_(4.5%) exhibited an intricate, flower-like morphology composed of hexagonal rod-like crystals radiating from the central core, signifying the evolution of nanostructures with varying preferential axes. The most prominent peak for nanorods was detected along the (101) direction.

Additionally, the nanoflowers displayed a non-vertical growth orientation, with predominant peaks identified as (100) and (002), substantiating the coherence of the SEM images. In contrast to the one-dimensional (1D) architecture of nanorods, the three-dimensional (3D) configuration of nanoflowers presented a superior surface-to-volume ratio, offering a competitive advantage in capturing additional light and enhancing sensitivity [55]. This expanded surface area is of paramount importance for photocatalytic applications. It was observed that the total surface area of nanoparticles exhibited an inverse relationship with their radius, with smaller nanospheres possessing a greater surface area than their larger counterparts. Nevertheless, nanorods featured a higher aspect ratio and an increased surface-to-volume ratio compared to nanospheres [56]. In summary, the synthesized nanoparticles' morphology is governed by many factors, encompassing laser irradiation techniques, environmental conditions, liquid media, laser beam spot size, and target materials (Figure 2).

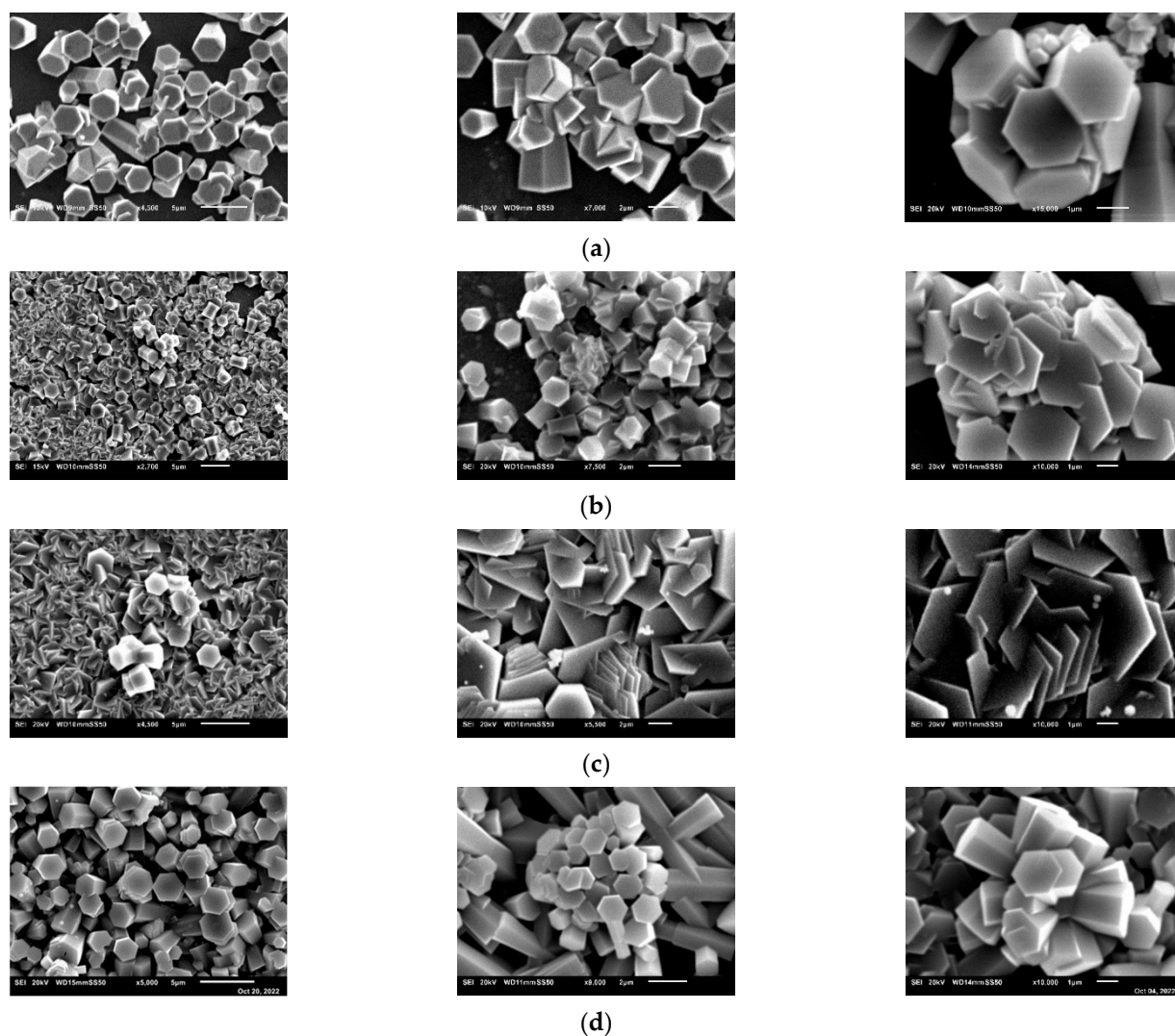


Figure 2. SEM images of samples (a) Pure ZnO, (b) ZnO:Ag_(1.5%), (c) ZnO:Ag_(3%), and (d) ZnO:Ag_(4.5%) synthesized by LACBS.

2.3. Energy Dispersive X-ray Diffractive (EDX)

The nanopowders, comprising pure ZnO, ZnO:Ag_(1.5%), ZnO:Ag_(3%), and ZnO:Ag_(4.5%), were synthesized utilizing the LACBS method and subsequently analyzed for their compositional characteristics via EDX analysis, as depicted in Figure 3. The assessment identified the presence of Zn, O, and Ag elements in the samples. The quantitative investigation revealed that pure ZnO maintained a 1:1 elemental ratio of zinc and oxygen, with respective concentrations of 50.04% and 49.96%, and exhibited an absence of impurities such as residual carbon. The Zn to oxygen ratio implied adequate oxygen vacancies within the sample. Table 2 delineates the elemental composition of the Ag-doped ZnO sample, which showed no additional impurities or residual peaks. These outcomes substantiate the successful synthesis of nanopowders with precise elemental composition and high purity using the LACBS technique.

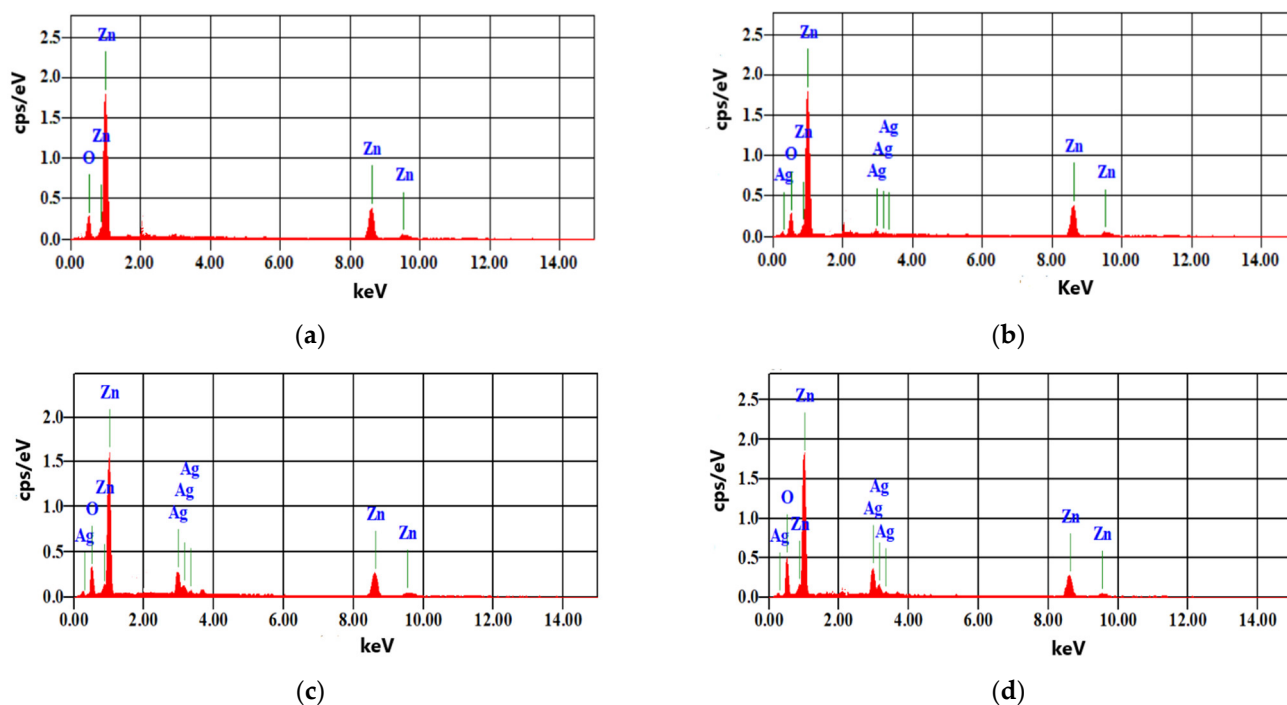


Figure 3. EDX spectra of samples (a) Pure ZnO, (b) ZnO:Ag_(1.5%), (c) ZnO:Ag_(3%), and (d) ZnO:Ag_(4.5%).

Table 2. EDX analysis of pure and Ag-doped ZnO nanoparticles.

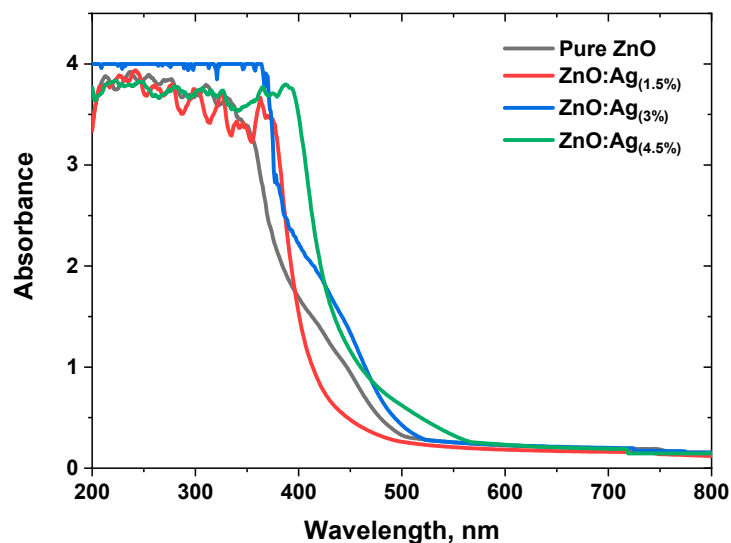
Samples	Pure ZnO		ZnO:Ag _(1.5%)		ZnO:Ag _(3%)		ZnO:Ag _(4.5%)	
	wt%	At%	wt%	At%	wt%	At%	wt%	At%
O	19.63	49.96	18.7	48.92	19.05	49.97	17.74	48.23
Zn	80.37	50.04	77.48	49.6	73.29	47.05	70.93	47.2
Ag	0	0	3.82	1.48	7.66	2.98	11.33	4.57
Total	100	100	100	100	100	100	100	100

2.4. UV-Vis Absorption

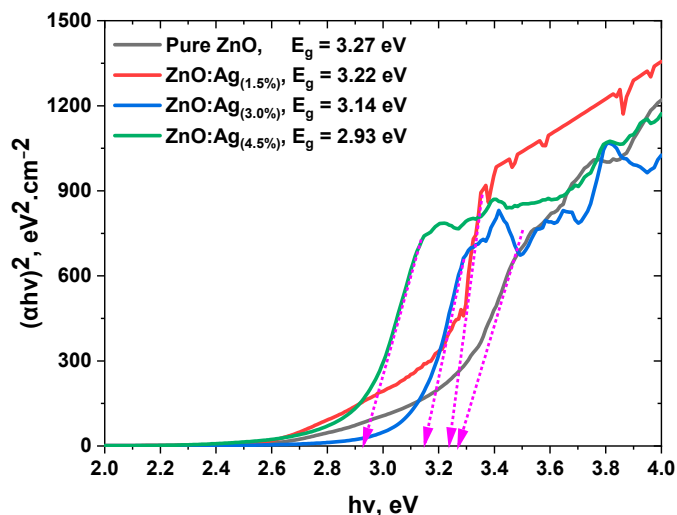
The optical band gaps of the synthesized samples, specifically pure ZnO, ZnO:Ag_(1.5%), ZnO:Ag_(3%), and ZnO:Ag_(4.5%), were scrutinized using UV-Visible absorption spectroscopy. Figure 4a exhibits their corresponding UV-Vis absorption spectra. The absorption edge of undoped ZnO at 384 nm resulted from electron transfer events occurring from the O^{2p} orbital to the Zn^{3d} orbital. The maximum absorption peak's shoulder originated from the critical electron transitions in ZnO, spanning from the valence band to the conduction band. Incorporating Al as a dopant induced a substantial redshift in the absorption edge, shifting toward higher wavelengths and leading to a reduced band gap. Figure 4b portrays the absorption edges of the samples. The optical band gaps of the nanostructured samples were ascertained using the UV-visible absorption spectra and the subsequent equations: Equations (7) and (8). Fundamental physical constants and parameters, such as Planck's constant (h), the speed of light (c), the maximum absorption wavelength (λ), the absorption coefficient (α), the absorption constant (A), and a dimensionless constant (n) that varies with the semiconductor type are all intricately connected to Equation (7), which represents the optical band gap in the context of semiconductor materials.

$$E_g(\text{eV}) = \frac{hc}{\lambda(\text{nm})} = \frac{1240}{\lambda(\text{nm})} \quad (7)$$

$$(\alpha h\nu)^n = A(h\nu - E_g) \quad (8)$$



(a)



(b)

Figure 4. (a) Absorbance spectra, and (b) Optical band gap of pure and Ag-doped ZnO nanostructures.

2.5. Fourier-Transform Infrared Spectra (FTIR)

The stretching mode of metal-oxygen bonds characteristically yields peaks within the 400 to 600 cm^{-1} range. Prior investigations have established that peaks encompassing 437 to 455 cm^{-1} furnish valuable information pertaining to the ZnO stretching vibration in hexagonal ZnO crystals [57]. The ZnO band is discernible at approximately 530 cm^{-1} in both undoped and Ag-doped ZnO nanostructures, as depicted in Figure 5. The peak spanning 3300 to 3700 cm^{-1} can be attributed to the O-H stretching of hydroxyl groups or water molecules adsorbed onto the nanoparticle surface. The lack of silver bands in the silver-modified ZnO spectra implies an absence of chemical linkage between silver and ZnO. The peak observed at 1500 cm^{-1} is associated with the bending vibrations of $\text{Zn}(\text{OH})_2$ as well as the stretching modes of symmetric and asymmetric C=O bonds. Furthermore, some bands identified during nanoparticle formation may be ascribed to the absorption of

airborne carbon dioxide and water moisture on the surface of metal cations, exhibiting a peak at approximately 2350 cm^{-1} [58].

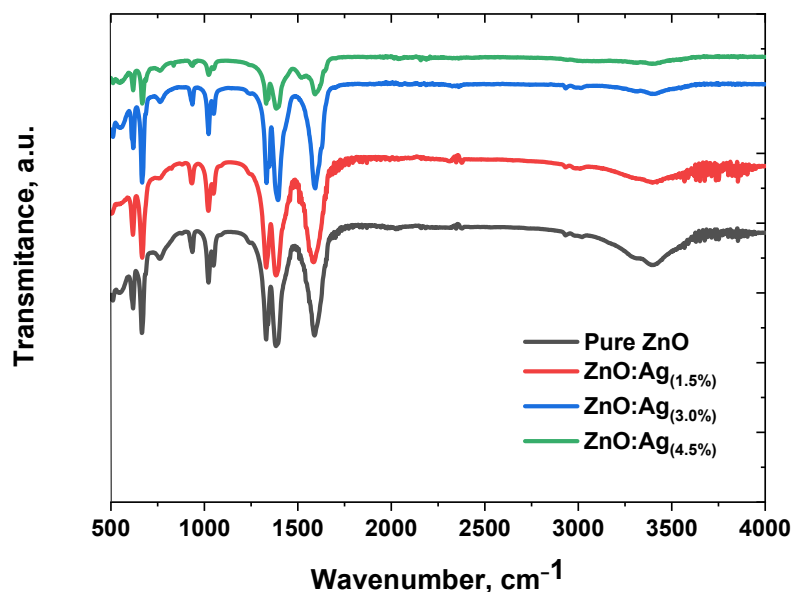


Figure 5. FTIR spectrum of pure and Ag-doped ZnO nanostructures.

2.6. Photocatalyst Study

2.6.1. Photocatalytic Degradation under Blue Laser Irradiation/UV–VIS Studies

Figure 6 presents a comprehensive analysis of the absorption spectra for both Methylene Blue (MB) and Methylene Orange (MO) dyes prior to and following exposure to a blue laser with a wavelength of 445 nm and a light intensity of 5.5 watts. The primary objective of this investigation was to evaluate the removal efficacy of pure and Ag-doped ZnO samples. Each ZnO sample exhibited remarkable photocatalytic activity when exposed to the blue laser, leading to a consistent attenuation of the MB spectra throughout the experiment. This observed reaction can be attributed to the generation and subsequent transportation of additional electron pairs to the surface, consequently yielding a higher concentration of hydroxyl radicals.

The degradation process was notably enhanced by the low band gap energy associated with the Ag-doped ZnO catalyst. This property contributed to an increase in oxygen defects and surface area, ultimately resulting in a more robust photocatalytic activity. Due to their superior performance, Ag-doped ZnO nanopowders hold significant potential for application in cost-effective and environmentally friendly pollutant remediation processes, requiring only a brief period for implementation. Figures 7 and 8 delineates the results of photocatalytic kinetics, which were employed to determine the dye degradation rate, represented by a plot of $\ln\left(\frac{C_0}{C}\right)$ as a function of time as shown in Figure 9.

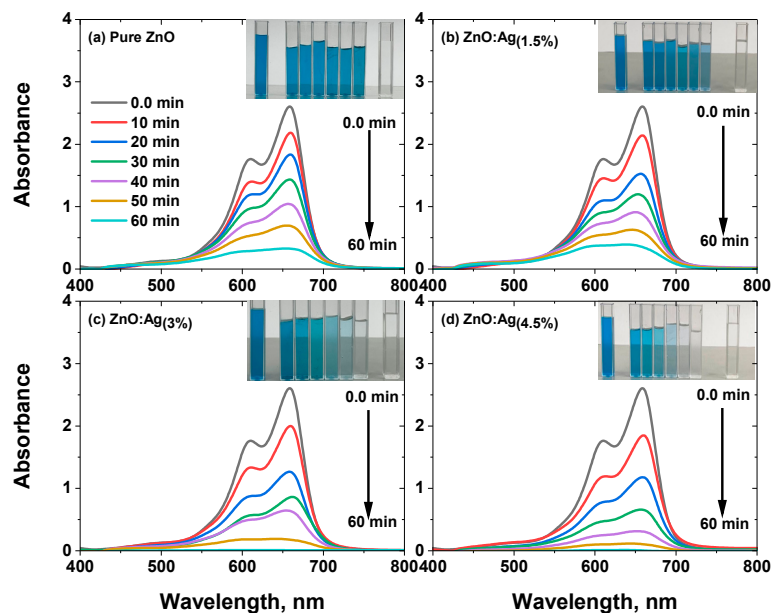
Table 3 presents a comparative analysis of recently developed ZnO photocatalysts, including both undoped and Ag-doped variants, and earlier studies focused on the oxidation of organic dyes. It is crucial to underscore the superior performance of the pure ZnO and Ag-doped ZnO photocatalysts compared to prior research outcomes. Moreover, it is pertinent to acknowledge the scarcity of scholarly work concerning utilizing ZnO and Ag-doped ZnO nano-photocatalysts in organic dye oxidation.

2.6.2. Photocatalyst Stability

The stability of a photocatalyst during light exposure is crucial for determining its potential practical applications. Photocatalysis is a process that accelerates photoreactions in the presence of a catalyst, relying on the generation of electron-hole pairs (e^- - h^+) that form free radicals such as O_2 and $(\cdot OH)$. The process entails the absorption of photons

by a semiconductor, followed by exciton generation and separating these excitons into electron-hole pairs.

(I)



(II)

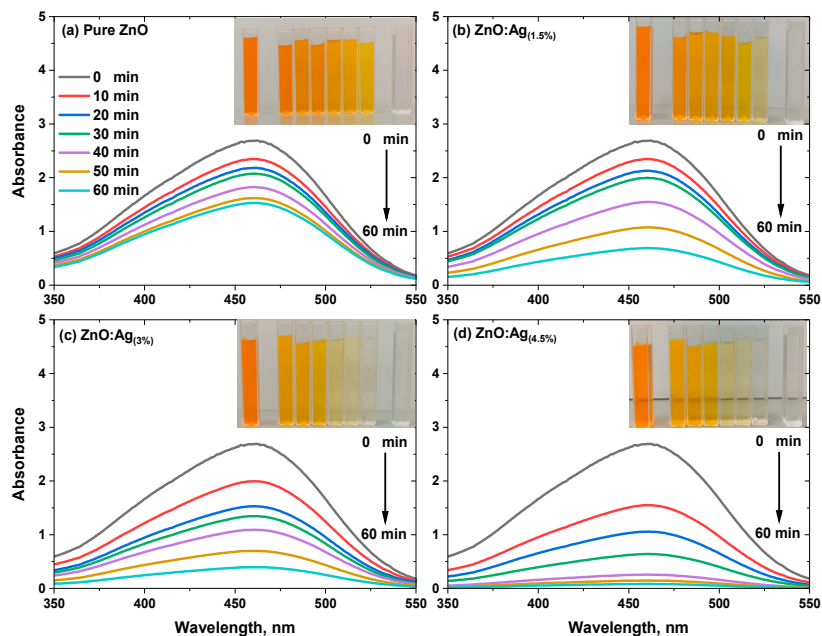


Figure 6. The UV-Visible absorption patterns of (I) MB and (II) MO dye examined using (a) Pure ZnO, (b) ZnO:Ag_(1.5%), (c) ZnO:Ag_(3%), and (d) ZnO:Ag_(4.5%).

This study conducted four photocatalytic tests using aged photocatalysts in fresh MB and MO solutions while maintaining a consistent overall catalyst concentration during blue laser exposure for the optimal sample, ZnO:Ag_(4.5%). The blue laser serves as the light source, providing the energy needed to initiate photocatalysis. The chosen wavelength is

critical, as it must align with the photocatalyst's bandgap to ensure efficient absorption and electron excitation. After each test cycle, the photocatalyst was centrifuged, washed with double-distilled water, and dried at 85 °C, while other parameters remained constant. This cleaning process is essential for removing potential impurities or residual dye from the photocatalyst surface, allowing for a clean catalyst at the beginning of each cycle. The photodegradation efficiency ($PDE\%$) was calculated using Equation (18) to quantify the degraded dye, as illustrated in Figure 10d. A slight decrease in photocatalytic degradation was observed with repeated testing, which may be due to a minor reduction in photocatalytic activity or changes in the catalyst surface from prolonged light exposure.

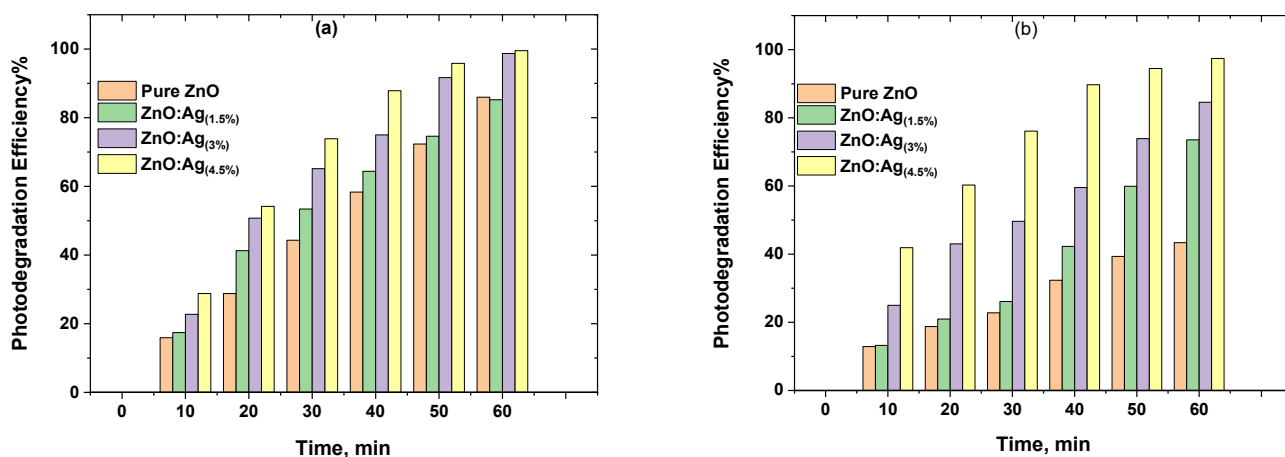


Figure 7. Degradation percentages of (a) MB and (b) MO dyes were measured at different time intervals and with varying photocatalysts.

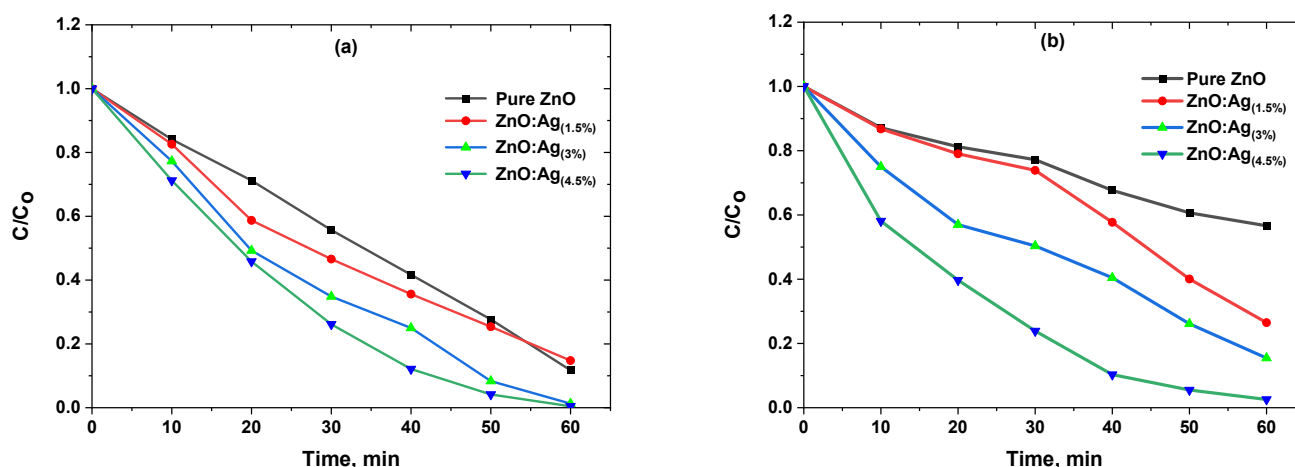


Figure 8. Concentration spectra of (a) MB and (b) MO using pure and Ag-doped ZnO nanostructures as a catalyst.

Figure 10c illustrates the dye adsorption of MB of values after 25 min of stirring under blue laser exposure were as follows: cycle 1 (99.67%), cycle 2 (98.12%), cycle 3 (97.63%), and cycle 4 (96.85%) while for MO they were: cycle 1 (97.39%), cycle 2 (96.74%), cycle 3 (95.32%), and cycle 4 (94.75%). The photocatalytic activity of the MB photocatalyst remained within a 96.9% range after four consecutive tests, whilst the MO photocatalyst remained with the range of 94.8%, suggesting their potential for water purification applications. The high $PDE\%$ can be attributed to the effective charge separation and enhanced photocatalytic performance resulting from the optimal ZnO and Ag combination.

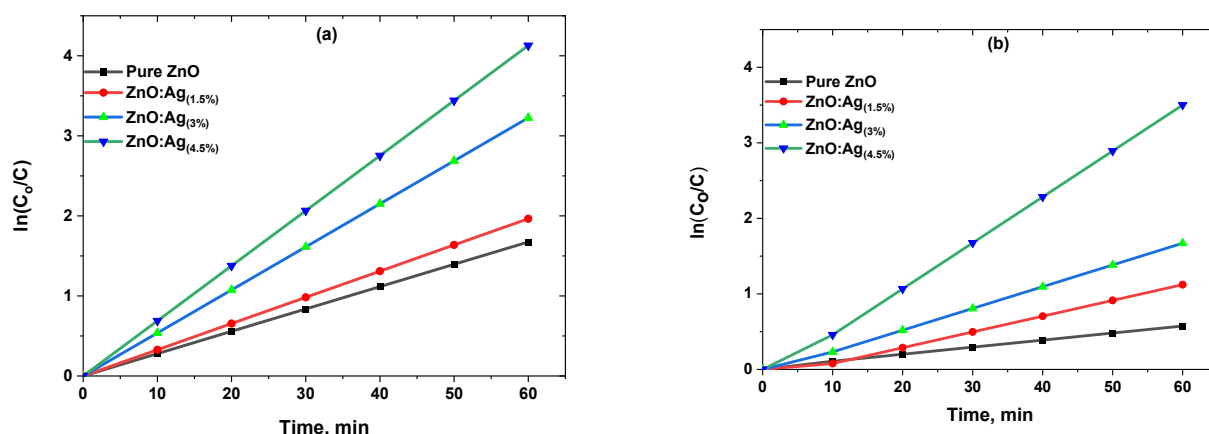


Figure 9. A time-dependent plot of $\ln\left(\frac{C_0}{C}\right)$ for calculating the rate constants of (a) MB and (b) MO.

Table 3. Comparison between efficiencies of different catalyst systems with earlier studies.

Synthesis Methods	Catalyst Types	Catalyst Amounts	Dyes	Light Sources	% Deg	k_{app} , (min ⁻¹)	Time, (min)	Ref.
Co-precipitation	ZnO:Ag _(0%)	25 mg/10 mg/L	MB (20 ppm)	Visible light	93	-	80	[59]
Hydrothermal	ZnO:Ag _(0.05–0.5%)	50 mg/50 ml	MB (10 ppm)	Sunlight	92.9	-	210	[60]
Co-precipitation	Ag-ZnO _(0–6%)	5 mg/50 ml	MB (10 ppm)	Visible light	98	-	120	[61]
LACBS	ZnO:Ag _(0%)	10 mg/50 mL	MB (20 ppm)	Blue	85.22	0.00934	60	This work
LACBS	ZnO:Ag _(1.5%)	10 mg/50 mL	MB (20 ppm)	Blue	85.98	0.02088	60	This work
LACBS	ZnO:Ag _(3%)	10 mg/50 mL	MB (20 ppm)	Blue	98.71	0.02878	60	This work
LACBS	ZnO:Ag _(4.5%)	10 mg/50 mL	MB (20 ppm)	Blue	99.54	0.06085	60	This work
Green combustion method	ZnO:Ag _(5%)	-	MO (20 ppm)	Visible light	94	-	80	[62]
LACBS	ZnO:Ag _(0%)	10 mg/50 mL	MO (20 ppm)	Blue	43.38	0.0164	60	This work
LACBS	ZnO:Ag _(1.5%)	10 mg/50 mL	MO (20 ppm)	Blue	73.53	0.02819	60	This work
LACBS	ZnO:Ag _(3%)	10 mg/50 mL	MO (20 ppm)	Blue	84.56	0.03782	60	This work
LACBS	ZnO:Ag _(4.5%)	10 mg/50 mL	MO (20 ppm)	Blue	97.43	0.05968	60	This work

The XRD pattern of the catalyst sample ZnO:Ag_(4.5%) after four cycles, displayed in Figure 10a, reveals phase stability, suggesting that the photocatalyst's chemical structure and composition were minimally affected during the degradation process. This observation is crucial, implying that the material can maintain its crystal structure and photocatalytic properties despite repeated use. The findings show that the synthesized sample represents a stable and reusable photocatalytic material for removing MB dye from water. This stability is particularly vital in large-scale applications, where long-term performance and recyclability are key factors in determining the viability of a photocatalyst for water purification.

Figure 10b showcases SEM imaging of the ZnO:Ag_(4.5%) photocatalyst sample, providing valuable insights into the material's morphology, particle size distribution, and surface characteristics concerning its stability. A detailed examination of the SEM images reveals a uniform and well-distributed nanostructure, which is crucial for maintaining the photocatalyst's stability over multiple cycles of the photodegradation process. The consistent microstructure, as evidenced by the SEM analysis, ensures the durability of the photocatalyst and its resistance to structural deterioration during extended light exposure. Moreover, the presence of Ag nanoparticles on the surface of ZnO can facilitate effective charge separation, reducing the recombination of electron-hole pairs and potentially improving the material's long-term stability. This is due to the reduced likelihood of undesired side reactions or structural changes that could compromise the photocatalyst's performance over time. The SEM imaging, therefore, not only confirms the successful synthesis of the ZnO:Ag_(4.5%) composite material but also provides supporting evidence for its stability as a photocatalyst. This stability is essential for large-scale water purification applications, where the photocatalyst's long-term performance and recyclability are key factors in determining its viability.

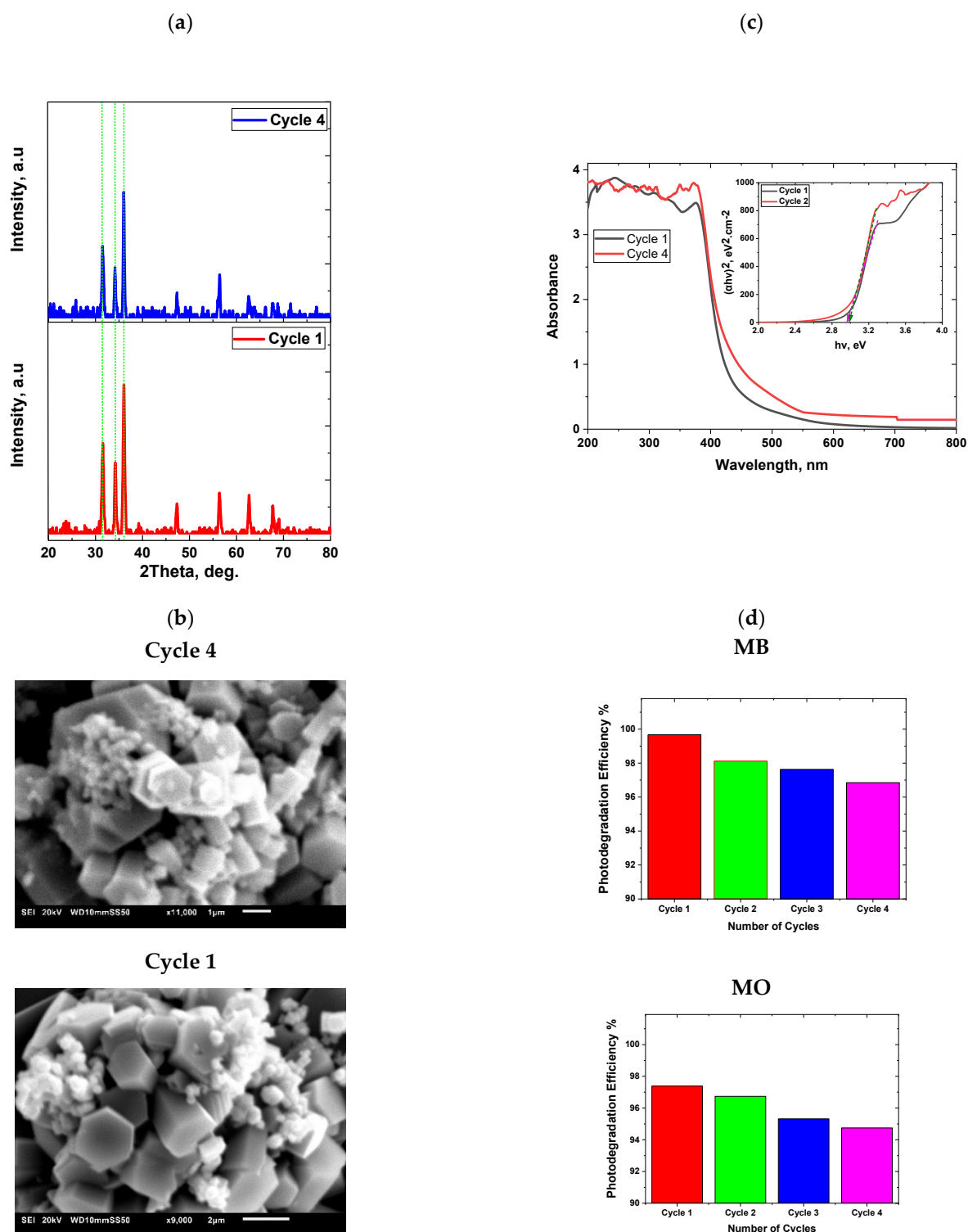


Figure 10. Photocatalyst stability studies.

2.6.3. The Mechanism of Photocatalyst

Figure 11 provides a schematic representation of the heterogeneous photocatalysis mechanism, a topic that has been the subject of extensive research due to its promising potential in addressing environmental pollution. The mechanism encompasses several critical steps, including the generation of photoinduced electron-hole pairs, their subsequent transfer across the semiconductor interface, and their interaction with adsorbed species [63].

Wide bandgap semiconductors, such as ZnO, have been the focus of numerous studies in this area, as they exhibit superior photocatalytic performance characterized by efficient electron-hole separation and high redox potentials. Despite these favorable attributes, the practical implementation of photocatalytic technology necessitates the development of advanced photocatalytic materials that demonstrate enhanced performance and stability under a wide range of environmental conditions.

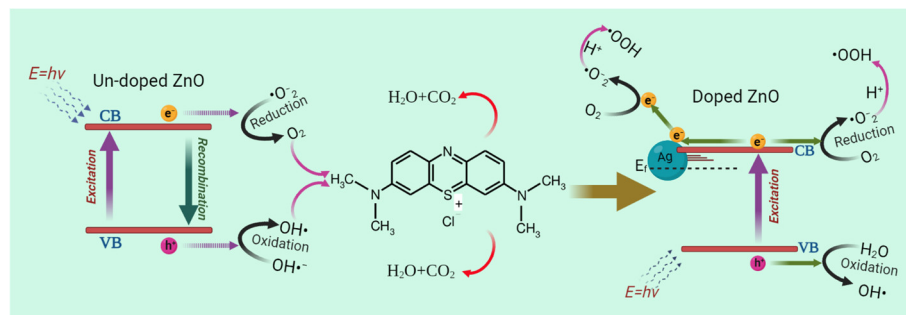
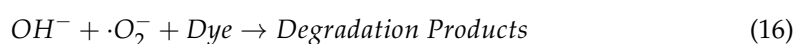
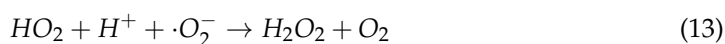
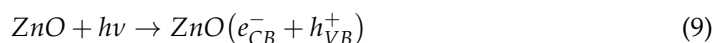


Figure 11. Schematic diagram of the proposed mechanism for the degradation of MB by Ag-doped ZnO nanostructures.

To address this challenge, noble metal-doped semiconductor nanoparticles have emerged as a promising strategy for augmenting photocatalytic activity. These materials have shown considerable potential by promoting charge transfer across the interface and facilitating the separation of photo-generated electrons and holes [64]. In particular, Ag-doped ZnO photocatalysts have attracted significant attention due to their exceptional photocatalytic performance and stability under various conditions.

Incorporating Ag into ZnO nanoparticles results in a local variation in the Fermi level, generating a potential energy gradient between the ZnO and Ag nanoparticles. This energy gradient enables the transfer of photo-generated electrons from the ZnO to the Ag nanoparticles [65,66]. Consequently, the electrons accumulate within the Ag nanoparticles, promoting the separation of photo-generated electrons and holes and ultimately leading to heightened photocatalytic efficiency. Moreover, the high electron storage capacity of Ag nanoparticles—attributable to their low work function and Fermi level—facilitates the transfer of electrons to adsorbed species, thereby contributing to the efficient degradation of pollutants [67,68].



2.7. Antimicrobial Activity of ZnO-NPs

The capacity to inhibit or eradicate microbial growth is a critical aspect of antimicrobial activity. Among various metal oxides, pure ZnO and Ag-doped ZnO have been identified as possessing exceptional antimicrobial properties against a diverse range of pathogens [31,69]. Notably, ZnO is particularly well-suited for antimicrobial applications due to its remarkable stability under harsh processing conditions and its relatively low toxicity levels [42,69].

2.7.1. ZOI of the Various Microorganisms

A thorough evaluation of the antimicrobial efficacy of ZnO-NPs synthesized using the LACBS method was conducted against five distinct microorganisms employing the ZOI technique. The results of this comprehensive analysis are presented in Table 4. The microorganisms subjected to testing included Gram-positive bacteria such as *Staphylococcus aureus* and *Bacillus subtilis*, Gram-negative bacteria like *Escherichia coli* and *Klebsiella pneumoniae*, as well as the yeast *Candida albicans*. To establish a baseline for comparison, positive control antibiotics gentamicin and nystatin were utilized for bacterial and fungal strains, respectively. In addition, negative controls consisting of ethanol and water were incorporated, which, as anticipated, produced no ZOI. The inhibitory effects of the LACBS-fabricated zinc oxide nanoparticles were quantified by measuring the ZOI in millimeters and subsequently comparing these findings to the results obtained with antibiotics.

Table 4. ZOI of Pure ZnO, ZnO-Ag_(1.5%), ZnO-Ag_(3%), and ZnO-Ag_(4.5%).

Pathogens	Antibiotics ^a	A ^b	Pure ZnO	ZnO-Ag _(1.5%)	ZnO-Ag _(3%)	ZnO-Ag _(4.5%)
<i>E. coli</i>	G	23	22	25	26	27
<i>S. aureus</i>	G	28	26	32	48	37
<i>Bacillus subtilis</i>	G	21	14	15	20	21
<i>K. pneumoniae</i>	G	30	35	34	40	45
<i>C. albicans</i>	NY	16	32	35	30	40

^a G = Gentamicin NY = Nystatin. All values are in mm and indicate ZOI, ^b ZOI of the positive control.

ZnO:Ag_(4.5%) demonstrated the most pronounced average zones of inhibition, with *K. pneumoniae* exhibiting the highest degree of inhibition at 45 mm, followed by *C. albicans* (40 mm), *S. aureus* (37 mm), *E. coli* (27 mm), and *B. subtilis* (21 mm). The second and third largest average inhibition zones were observed in the cases of ZnO:Ag_(1.5%) and ZnO:Ag_(3%), respectively. Conversely, pure ZnO revealed the least expansive average inhibition zones. Notably, *K. pneumoniae* (35 mm) and *C. albicans* (32 mm) presented larger inhibition zones compared to those generated by conventional antibiotics. In contrast, *S. aureus* (26 mm), *E. coli* (22 mm), and *B. subtilis* (14 mm) displayed no substantial inhibition when juxtaposed with the ZOI attributed to gentamicin (Table 4, Figure 12).

2.7.2. Comparison between Our Findings and Prior Investigations

These results corroborate earlier research, which has established the antimicrobial efficacy of zinc oxide against a diverse range of pathogens. Notably, the LACB-synthesized zinc oxide displayed a substantially enhanced zone of inhibition (ZOI) against these pathogens, underscoring its considerable potential as a formidable contender for forthcoming antimicrobial applications (Table 5).

2.7.3. The Antimicrobial Mechanisms of Zinc Oxide Nanoparticles

ZnO-NPs demonstrate a variety of antimicrobial pathways, as illustrated in Figure 13. The proposed mechanisms encompass the generation of reactive oxygen species (ROS), including superoxide anion (O₂⁻), hydroxyl radicals (OH⁻), and hydrogen peroxide (H₂O₂). These ROS induce oxidative stress, damaging vital cellular components such as DNA and lipids, ultimately culminating in cellular demise. Concurrently, silver nanoparticles

(Ag-NPs) exhibit antimicrobial properties, engaging with bacterial cells through an array of mechanisms.

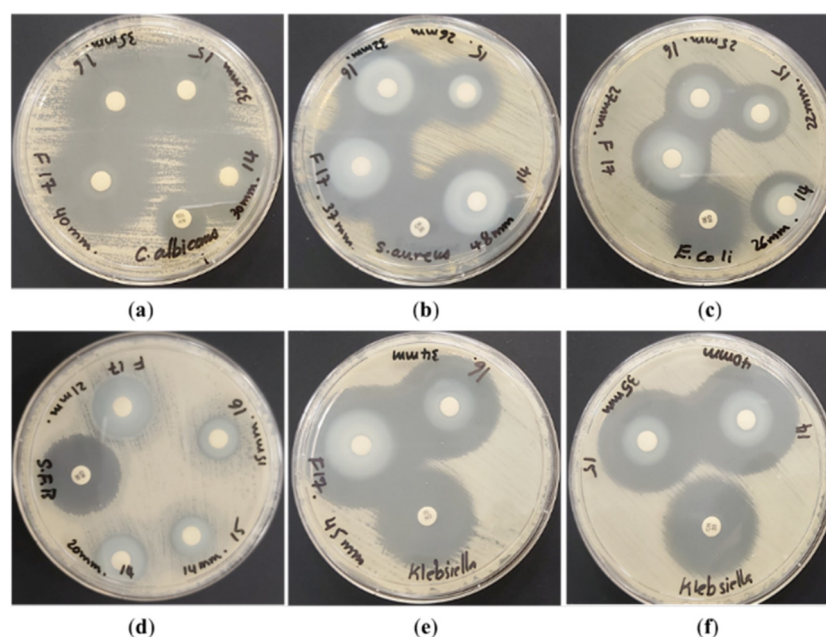


Figure 12. Positive control antibiotics and, from left to right, Pure ZnO, ZnO:Ag_(1.5%), ZnO:Ag_(3%), and ZnO:Ag_(4.5%), were tested against (a) *C. albicans*, (b) *S. aureus*, (c) *E. coli*, (d) *Bacillus subtilis*, and (e,f) *K. pneumonia*.

Table 5. Comparison of ZOI across multiple studies.

Pathogens	Materials	ZOI (mm)	Ref.
<i>E. coli</i>	ZnO-Ag _(4.5%)	27	This study
	Ag-ZnO-NPs	21	[41]
	ZnO-Ag _(5%)	R ^a	[70]
<i>S. aureus</i>	ZnO-Ag _(4.5%)	37	This study
	Ag-ZnO-NPs	19	[41]
	ZnO-Ag _(5%)	14	[70]
<i>Bacillus subtilis</i>	ZnO-Ag _(4.5%)	21	This study
	RGO-ZnO	28.8	[71]
<i>K. pneumonia</i>	ZnO-Ag _(4.5%)	45	This study
	Cu-doped ZnO-NP	17	[72]
	Al-doped ZnO	10	[73]
<i>C. albicans</i>	ZnO-Ag _(4.5%)	40	This study
	Pure ZnO	7.66	[38]

^a Resistant.

ZnO-NPs and Ag-NPs produce ROS, which instigate oxidative stress in microorganisms and disrupt crucial cellular functions [74]. The release of silver ions (Ag⁺) from Ag-NPs interacts with bacterial cell membranes, consequently augmenting membrane permeability and facilitating the leakage of intracellular contents [75]. This interaction not only distorts the plasma membrane structure but also interferes with metabolic functions, leading to the leakage of intracellular contents, akin to the effects observed in ZnO-NPs [43,76]. Additionally, Ag⁺ ions possess the ability to bind to bacterial proteins and enzymes, thereby inhibiting their activity and perturbing essential metabolic processes [77], an outcome reminiscent of the impact of Zn²⁺ ions released from ZnO-NPs. Moreover, silver ions have been implicated in disrupting bacterial DNA replication, hindering cell division, and inhibiting bacterial growth [78].

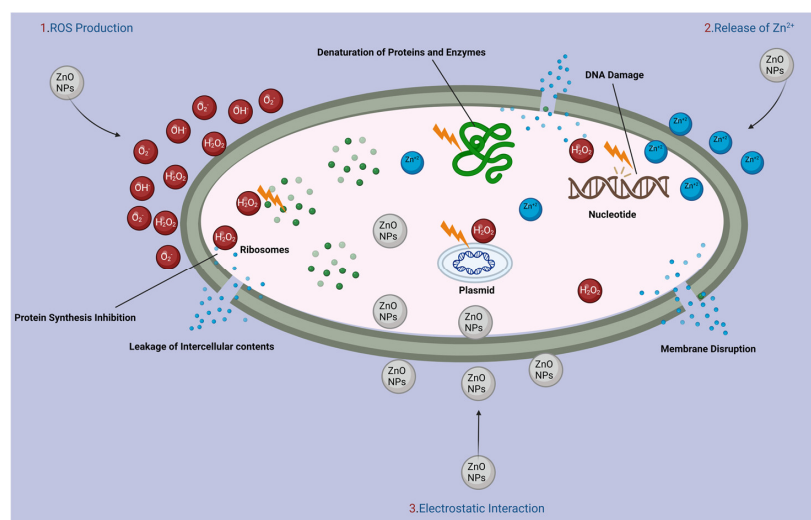


Figure 13. An illustration of the various antimicrobial mechanisms of ZnO.

3. Materials and Methods

3.1. Starting Materials and Microbial Strain Culture Preparation

High-purity analytical-grade reagents, including zinc acetate dihydrate [$\text{Zn}(\text{CH}_3\text{COO})_2(\text{H}_2\text{O})_2$ ($\geq 99.99\%$)] and hexamethylenetetramine [$\text{C}_6\text{H}_{12}\text{N}_4$ (99.9%)], were procured from Sigma Aldrich, St. Louis, MO, USA and utilized without additional refinement. Silver nitrate (AgNO_3) was supplied also by Sigma Aldrich, St. Louis, MO, USA, while MB [$\text{C}_{16}\text{H}_{18}\text{ClN}_3\text{S}$] and MO [$\text{C}_{14}\text{H}_{14}\text{N}_3\text{NaO}_3\text{S}$] were acquired from Merck, United States. Deionized water served as the deposition solvent for precursor solutions. Sabouraud Dextrose Broth, Mueller-Hinton Broth, and a variety of microbial strains, including *Escherichia coli* (WDCM 00013), *Klebsiella pneumoniae* (WDCM 00097), *Candida albicans* (WDCM 00054), *Bacillus subtilis* (WDCM 00003), and *Staphylococcus aureus* (ATCC 25923), were sourced from Sigma Aldrich St. Louis, MO, USA and Liofilchem, Via Scozia, TE, Italy. The microorganisms were preserved at $-20\text{ }^\circ\text{C}$ and subsequently cultured in Mueller-Hinton Broth prior to experimentation. Sterile filter paper discs (6 mm diameter) were obtained from Himedia Jaitala Nagpur, India, while disposable sterilized Petri dishes with Mueller-Hinton II agar, McFarland standard sets, gentamicin $30\text{ }\mu\text{g}/\text{disc}$ (Ref. # 9125), and nystatin $100\text{ IU}/\text{disc}$ (Ref. # 9078) were supplied by Liofilchem, Via Scozia, TE, Italy.

3.2. Catalyst Preparation

To achieve a 0.2 M concentration, three distinct solutions were prepared in volumetric flasks. Solution A consisted of 2.195 g of hexamethylenetetramine ($\text{C}_6\text{H}_{12}\text{N}_4$) dissolved in 50 mL of deionized water. Solution B was formulated by dissolving 1.401 g of zinc acetate ($\text{ZnC}_4\text{H}_6\text{O}_4$) in 50 mL of deionized water, and Solution C was generated by dissolving 1.698 g of silver nitrate (AgNO_3) in 50 mL of deionized water. All solutions were subsequently stirred vigorously and sonicated to ensure complete dissolution and homogeneity.

3.3. Synthesis of Pure and Silver-Doped Zinc Oxide Nanostructures via the LACBS Method

The LACBS method was employed to fabricate both pure ZnO nanopowder and Ag-doped ZnO nanostructures. For the synthesis of pure ZnO nanopowder, precursor solutions A and B were separately prepared by dissolving them through magnetic stirring for 20 min at room temperature. Following this, solution B was incrementally introduced to solution A while maintaining continuous stirring for an additional 25 min at room temperature, ensuring a homogenous mixture. During the synthesis process, a continuous-wave semiconductor blue laser ($\lambda = 445\text{ nm}$ and $P = 5.5\text{ W}$) was directed vertically onto the combined solution, which was concurrently subjected to magnetic swirling for two hours at $65\text{ }^\circ\text{C}$ to foster uniform growth of nanostructures. The resultant precipitate was

subsequently filtered and rinsed quadruple times using ethanol and distilled water. The ZnO nanostructures were then dried at 105 °C for 60 min and annealed at 420 °C for 4 h to eliminate residual organic materials.

In the case of Ag-doped ZnO nanostructures synthesis, solutions A, B, and C were prepared independently through magnetic stirring at room temperature for 20 min. Distinct concentrations of Ag-doped ZnO were synthesized by incorporating an appropriate quantity of silver nitrate (AgNO_3) while employing the aforementioned method. Figure 14 comprehensively depicts the synthesis process for both pure and Ag-doped ZnO nanostructures.

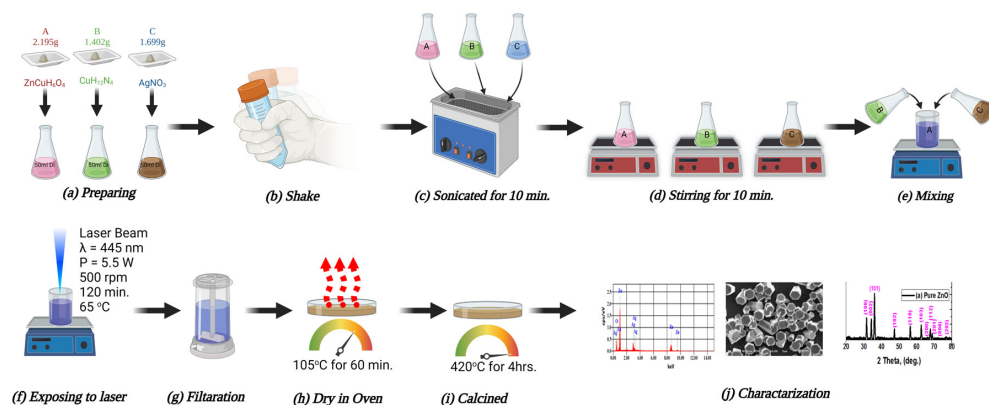


Figure 14. Schematic diagram and illustration of the working principle for synthesizing pure and Ag-doped ZnO nanostructures.

3.4. Photocatalytic Study

To meticulously investigate the photocatalytic degradation of MB and MO dyes while circumventing any potential interference from thermal catalysis, a series of experiments were conducted under carefully controlled conditions at room temperature. A blue laser light source with a wavelength of 445 nm was employed to ensure optimal photocatalytic activity. A solution with a concentration of 20 ppm MB was treated with 10 mg of the synthesized catalysts and stirred continuously. The mixture was subsequently agitated in the absence of light for a duration of 15 min, which facilitated the establishment of an adsorption-desorption equilibrium. The mixture was then exposed to blue laser irradiation, and 5 mL aliquots of the solution were extracted at 10-min intervals for further analysis. An identical procedure was implemented for the MO dye.

The extracted samples were then examined thoroughly using a UV/Vis spectrophotometer, which revealed maximum absorption values of 656.4 nm for MB and 461.2 nm for MO. Employing Equations (17) and (18) as previously reported in the literature [58,59], the degree of dye degradation, apparent degradation rate (k_{app}), and photodegradation efficiency ($PDE\%$) were systematically calculated. C_0 and C denote the MB concentration at the initial time and at a specific time t post-irradiation, respectively. A comprehensive schematic diagram illustrating the methodological approach of the photocatalytic investigation is presented in Figure 15.

$$\ln \frac{C_0}{C} = k_{app}t \quad (17)$$

$$PDE\% = \left(1 - \frac{C}{C_0}\right) \times 100\% \quad (18)$$

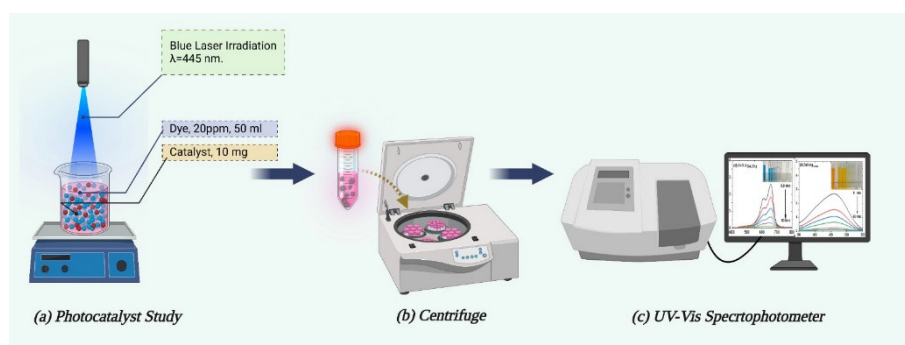


Figure 15. Schematic diagram and illustration of the working principles.

3.5. Characterization and Evaluation of Antimicrobial Efficacy of Zinc Oxide Nanostructures

A comprehensive analysis was conducted to investigate the crystalline nature of pure and Ag-doped ZnO nanostructures using an XRD for precise phase and structure identification. A field emission scanning electron microscope (FE-SEM, JEOL-JSM-7600F) equipped with EDX was employed to thoroughly examine the surface morphology and elemental composition of the prepared nanostructures. The optical absorbance of the materials was meticulously assessed using a UV-Visible spectrometer model P.E. Lambda 750S, and the optical absorption spectra of the samples were corroborated using a UV-Vis spectrum analyzer. FTIR was utilized to provide an in-depth analysis of the chemical composition of the molecules. The study extensively explored the impact of LACBS-synthesized ZnO on the growth of one fungal strain (*C. albicans*) and four bacterial strains, encompassing two Gram-positive strains (*S. aureus* and *B. subtilis*) and two Gram-negative strains (*E. coli* and *K. pneumonia*). The disc diffusion method was employed to accurately determine the ZOI, using gentamicin as a positive control for all bacterial strains and nystatin for the fungal strain, *C. albicans*. Negative controls, such as the solvent (water), were excluded from the study due to their lack of inhibition zones.

3.6. Disc Diffusion Method and Zone of Inhibition (ZOI)

The current study aimed to rigorously assess the antimicrobial properties of zinc oxide synthesized using LACBS, following the Clinical and Laboratory Standards Institute guidelines [79]. The bacteria were cultured in Mueller Hinton Broth at 37 °C for a minimum of 4 h, while *C. albicans* was cultured in Sabouraud Dextrose broth at 30 °C. Sterile cotton swabs were employed to uniformly distribute 100 µL of the microbial culture onto sterile Petri dishes containing Mueller Hinton Agar, which were subsequently allowed to dry for 10 min. Nystatin and gentamicin antibiotic discs functioned as controls. Filter paper discs impregnated with nanocolloids containing 1 mL of each powder were immersed under ambient conditions and left to dry for 24 h. The diameter of the unobstructed ZOI surrounding the disc was meticulously measured to the nearest millimeter using a ruler. A ZOI of zero indicated resistance to the treatment, while the presence of an inhibition zone suggested susceptibility.

4. Conclusions

Recent studies have been increasingly focused on discovering alternative antimicrobial treatments due to the rapid emergence of drug-resistant microorganisms. A particularly promising solution is the utilization of Ag-doped ZnO nanoparticles, which exhibit remarkable antimicrobial efficacy against a wide range of pathogens. These nanoparticles have been synthesized employing an innovative, cost-effective, and straightforward technique known as LACBS, which facilitates the production of both pure and Ag-doped ZnO nanostructures. The influence of Ag doping concentration has been thoroughly examined on the material's structural, optical, and antimicrobial properties by utilizing an array of analytical methods, including XRD, SEM, EDS, UV-Vis, FTIR, and ZOI tests. In addition to their potent antimicrobial properties, these ZnO photocatalytic materials demonstrate exceptional

performance in degrading MB and MO. The incorporation of Ag plays a crucial role in expediting interfacial charge transfer processes, thereby augmenting the photocatalytic activity of these materials. This observation emphasizes the substantial contribution of silver to the electron-trapping capabilities of Ag-doped ZnO submicron structures. Moreover, the development of a visible-light-responsive photocatalyst presents a promising avenue for expanding the range of applications for these materials. In summary, this research underscores the potential of Ag-doped ZnO nanoparticles synthesized using the LACBS method as an effective, broad-spectrum microbicidal and disinfectant solution to counteract drug-resistant microbial threats.

Author Contributions: Conceptualization, S.H.Z. and A.H.Z.; methodology, S.H.Z. and I.S.Y.; software, M.G.D. and G.N.M.; validation, S.H.Z., S.O.A. and O.E.H.; formal analysis, S.H.Z., S.O.A., O.E.H., A.J. and H.Y.Z.; investigation, S.H.Z., S.O.A. and O.E.H.; resources, S.H.Z., M.S., N.H. and N.Q.; data curation, S.H.Z., S.O.A., O.E.H., H.A.S., S.H.B. and A.A.; writing—original draft preparation, S.H.Z., S.O.A., O.E.H., G.N.M. and M.S.A.-w.; writing—review and editing, S.H.Z., S.O.A., O.E.H., M.S.A.-w. and I.S.Y.; visualization, N.H.; supervision, S.H.Z.; project administration, S.H.Z.; funding acquisition, S.H.Z. All authors have read and agreed to the published version of the manuscript.

Funding: This work was kindly supported by the Deanship of Graduate Studies and Research, Ajman University, Ajman, UAE, for the financial assistance through Grant number (Project ID, DGSR Ref. Number: 2022-IRG-HBS-1). The authors extend their appreciation to the Deanship of Scientific Research at King Khalid University for funding this work through the large research group program number: R.G.P.2/434/44.

Data Availability Statement: All data are contained within the article.

Acknowledgments: The authors express their profound gratitude to Taimoor Ahmad, and Sohaib Naseem Khan from Ajman University for generously providing their expertise and conducting the FTIR analysis and the synthesis of nanoparticles, which significantly enhanced the quality of our research. Additionally, we extend our sincerest appreciation to Bayan Alradi, Bashayer Al Maamari, and Jamil Hassan Al Alami from Ajman University for their diligent efforts in collecting the photocatalyst data, which were integral to the successful completion of this study. Furthermore, we would like to thank Abdul Razack Hajamohideen from United Arab Emirates University for his invaluable contributions to our research through his provision of the SEM and XRD analyses. The expertise and hard work of these individuals have undoubtedly enriched our research and aided us in achieving our scientific objectives.

Conflicts of Interest: The authors declare no conflict of interest.

References

1. Godman, B.; Egwuenu, A.; Wesangula, E.; Schellack, N.; Kalungia, A.C.; Tiroyakgosi, C.; Kgatlwane, J.; Mwita, J.C.; Patrick, O.; Niba, L.L.; et al. Tackling antimicrobial resistance across sub-Saharan Africa: Current challenges and implications for the future. *Expert Opin. Drug Saf.* **2022**, *21*, 1089–1111. [[CrossRef](#)]
2. Pulingam, T.; Parumasivam, T.; Gazzali, A.M.; Sulaiman, A.M.; Chee, J.Y.; Lakshmanan, M.; Chin, C.F.; Sudesh, K. Antimicrobial resistance: Prevalence, economic burden, mechanisms of resistance and strategies to overcome. *Eur. J. Pharm. Sci.* **2022**, *170*, 106103. [[CrossRef](#)]
3. Abushaheen, M.A.; Muzahed; Fatani, A.J.; Alosaimi, M.; Mansy, W.; George, M.; Acharya, S.; Rathod, S.; Divakar, D.D.; Jhugroo, C.; et al. Antimicrobial resistance, mechanisms and its clinical significance. *Dis. Mon.* **2020**, *66*, 100971. [[CrossRef](#)]
4. Di, K.N.; Pham, D.T.; Tee, T.S.; Binh, Q.A.; Nguyen, T.C. Antibiotic usage and resistance in animal production in Vietnam: A review of existing literature. *Trop. Anim. Health Prod.* **2021**, *53*, 340. [[CrossRef](#)] [[PubMed](#)]
5. Hernando-Amado, S.; Coque, T.M.; Baquero, F.; Martínez, J.L. Defining and combating antibiotic resistance from One Health and Global Health perspectives. *Nat. Microbiol.* **2019**, *4*, 1432–1442. [[CrossRef](#)]
6. Hu, Y.; Anes, J.; Devineau, S.; Fanning, S. Klebsiella pneumoniae: Prevalence, Reservoirs, Antimicrobial Resistance, Pathogenicity, and Infection: A Hitherto Unrecognized Zoonotic Bacterium. *Foodborne Pathog. Dis.* **2021**, *18*, 63–84. [[CrossRef](#)]
7. Tyrrell, C.; Burgess, C.M.; Brennan, F.P.; Walsh, F. Antibiotic resistance in grass and soil. *Biochem. Soc. Trans.* **2019**, *47*, 477–486. [[CrossRef](#)] [[PubMed](#)]
8. Subramaniam, G.; Girish, M. Antibiotic Resistance—A Cause for Reemergence of Infections. *Indian J. Pediatr.* **2020**, *87*, 937–944. [[CrossRef](#)]
9. Wyres, K.L.; Lam, M.M.C.; Holt, K.E. Population genomics of Klebsiella pneumoniae. *Nat. Rev. Microbiol.* **2020**, *18*, 344–359. [[CrossRef](#)]

10. Colomb-Cotinat, M.; Lacoste, J.; Brun-Buisson, C.; Jarlier, V.; Coignard, B.; Vaux, S. Estimating the morbidity and mortality associated with infections due to multidrug-resistant bacteria (MDRB), France, 2012. *Antimicrob. Resist. Infect. Control* **2016**, *5*, 56. [CrossRef] [PubMed]
11. Dadgostar, P. Antimicrobial Resistance: Implications and Costs. *Infect. Drug Resist.* **2019**, *12*, 3903–3910. [CrossRef]
12. Drug-Resistant Infections: A Threat to Our Economic Future. 2017. Available online: <https://elibrary.worldbank.org/doi/abs/10.1596/26707> (accessed on 4 March 2023).
13. Buckley, G.J.; Palmer, G.H. *Combating Antimicrobial Resistance and Protecting the Miracle of Modern Medicine*; The National Academies Press: Washington, DC, USA, 2022; pp. 1–366. [CrossRef]
14. Murray, C.J.; Ikuta, K.S.; Sharara, F.; Swetschinski, L.; Aguilar, G.R.; Gray, A.; Han, C.; Bisignano, C.; Rao, P.; Wool, E.; et al. Global burden of bacterial antimicrobial resistance in 2019: A systematic analysis. *Lancet* **2022**, *399*, 629–655. [CrossRef]
15. Mancuso, G.; Midiri, A.; Gerace, E.; Biondo, C. Bacterial Antibiotic Resistance: The Most Critical Pathogens. *Pathogens* **2021**, *10*, 1310. [CrossRef] [PubMed]
16. Centers for Disease Control and Prevention. Antibiotic Resistance Threats in the United States, 2013. CDC 2013, 55–56. Available online: <https://www.cdc.gov/drugresistance/pdf/ar-threats-2013-508.pdf> (accessed on 4 March 2023).
17. Toda, M.; Williams, S.R.; Berkow, E.L.; Farley, M.M.; Harrison, L.H.; Bonner, L.; Marceaux, K.M.; Hollick, R.; Zhang, A.Y.; Schaffner, W.; et al. Population-Based Active Surveillance for Culture-Confirmed Candidemia—Four Sites, United States, 2012–2016. *MMWR Surveill. Summ.* **2020**, *68*, 1–17. [CrossRef] [PubMed]
18. Crowe-McAuliffe, C.; Graf, M.; Huter, P.; Takada, H.; Abdelshahid, M.; Nováček, J.; Murina, V.; Atkinson, G.C.; Haurlyuk, V.; Wilson, D.N. Structural basis for antibiotic resistance mediated by the *Bacillus subtilis* ABCF ATPase VmlR. *Proc. Natl. Acad. Sci. USA* **2018**, *115*, 8978–8983. [CrossRef]
19. Sholeh, M.; Krutova, M.; Forouzesh, M.; Mironov, S.; Sadeghifard, N.; Molaeipour, L.; Maleki, A.; Kouhsari, E. Antimicrobial resistance in *Clostridioides (Clostridium) difficile* derived from humans: A systematic review and meta-analysis. *Antimicrob. Resist. Infect. Control* **2020**, *9*, 158. [CrossRef] [PubMed]
20. Koop, S.H.A.; van Leeuwen, C.J. The challenges of water, waste and climate change in cities. *Environ. Dev. Sustain.* **2017**, *19*, 385–418. [CrossRef]
21. Boukhessaim, S.; Gacem, A.; Khan, S.H.; Amari, A.; Yadav, V.K.; Harharah, H.N.; Elkhaleefa, A.M.; Yadav, K.K.; Rather, S.U.; Ahn, H.J.; et al. Emerging Trends in the Remediation of Persistent Organic Pollutants Using Nanomaterials and Related Processes: A Review. *Nanomaterials* **2022**, *12*, 2148. [CrossRef]
22. Lutchmiah, K.; Verliefd, A.R.D.; Roest, K.; Rietveld, L.C.; Cornelissen, E.R. Forward osmosis for application in wastewater treatment: A review. *Water Res.* **2014**, *58*, 179–197. [CrossRef] [PubMed]
23. Garrido-Cardenas, J.A.; Esteban-García, B.; Agüera, A.; Sánchez-Pérez, J.A.; Manzano-Agugliaro, F. Wastewater Treatment by Advanced Oxidation Process and Their Worldwide Research Trends. *Int. J. Environ. Res. Public Health* **2019**, *17*, 170. [CrossRef]
24. Majumder, M.A.A.; Rahman, S.; Cohall, D.; Bharatha, A.; Singh, K.; Haque, M.; Gittens-St Hilaire, M. Antimicrobial Stewardship: Fighting Antimicrobial Resistance and Protecting Global Public Health. *Infect. Drug Resist.* **2020**, *13*, 4713–4738. [CrossRef] [PubMed]
25. Wise, R. The development of new antimicrobial agents. *BMJ* **1998**, *317*, 643–644. [CrossRef]
26. Manyi-Loh, C.; Mamphweli, S.; Meyer, E.; Okoh, A. Antibiotic Use in Agriculture and Its Consequential Resistance in Environmental Sources: Potential Public Health Implications. *Molecules* **2018**, *23*, 795. [CrossRef]
27. Hariyanto, H.; Yahya, C.Q.; Cucunawangsih, C.; Pertiwi, C.L.P. Antimicrobial resistance and mortality. *Afr. J. Infect. Dis.* **2022**, *16*, 13–20. [CrossRef]
28. Frost, L.; Van Boeckel, T.P.; Pires, J.; Craig, J.; Laxminarayan, R. Global geographic trends in antimicrobial resistance: The role of international travel. *J. Travel Med.* **2019**, *26*, taz036. [CrossRef]
29. Zyoud, S.H.; Yahia, I.S.; Shahwan, M.; Zyoud, A.H.; Zahran, H.Y.; Abdel-wahab, M.S.; Daher, M.G.; Nador, M.; Makhadmeh, G.N.; Hassan, N.; et al. Fast and Excellent Enhanced Photocatalytic Degradation of Methylene Blue Using Silver-Doped Zinc Oxide Submicron Structures under Blue Laser Irradiation. *Crystals* **2023**, *13*, 229. [CrossRef]
30. Seil, J.T.; Webster, T.J. Antimicrobial applications of nanotechnology: Methods and literature. *Int. J. Nanomed.* **2012**, *7*, 2767. [CrossRef]
31. Rajendran, R.; Mani, A. Photocatalytic, antibacterial and anticancer activity of silver-doped zinc oxide nanoparticles. *J. Saudi Chem. Soc.* **2020**, *24*, 1010–1024. [CrossRef]
32. Tereshchenko, A.; Bechelany, M.; Viter, R.; Khranovskyy, V.; Smyntyna, V.; Starodub, N.; Yakimova, R. Optical biosensors based on ZnO nanostructures: Advantages and perspectives. A review. *Sens. Actuators B Chem.* **2016**, *229*, 664–677. [CrossRef]
33. Qin, L.; Mawignon, F.J.; Hussain, M.; Ange, N.K.; Lu, S.; Hafezi, M.; Dong, G. Economic Friendly ZnO-Based UV Sensors Using Hydrothermal Growth: A Review. *Materials* **2021**, *14*, 4083. [CrossRef] [PubMed]
34. Aftab, S.; Shabir, T.; Shah, A.; Nisar, J.; Shah, I.; Muhammad, H.; Shah, N.S. Highly Efficient Visible Light Active Doped ZnO Photocatalysts for the Treatment of Wastewater Contaminated with Dyes and Pathogens of Emerging Concern. *Nanomaterials* **2022**, *12*, 486. [CrossRef]
35. Lemos, S.C.S.; de Lima Rezende, T.K.; Assis, M.; da Costa Romeiro, F.; Peixoto, D.A.; de Oliveira Gomes, E.; Jacobsen, G.M.; Teodoro, M.D.; Gracia, L.; Ferrari, J.L.; et al. Efficient Ni and Fe doping process in ZnO with enhanced photocatalytic activity: A theoretical and experimental investigation. *Mater. Res. Bull.* **2022**, *152*, 111849. [CrossRef]

36. Lallo da Silva, B.; Abuçafy, M.P.; Berbel Manaia, E.; Oshiro Junior, J.A.; Chiari-Andréo, B.G.; Pietro, R.C.R.; Chiavacci, L.A. Relationship between Structure and Antimicrobial Activity of Zinc Oxide Nanoparticles: An Overview. *Int. J. Nanomed.* **2019**, *14*, 9395. [[CrossRef](#)] [[PubMed](#)]
37. Mendes, C.R.; Dilarri, G.; Forsan, C.F.; Sapata, V.D.M.R.; Lopes, P.R.M.; de Moraes, P.B.; Montagnolli, R.N.; Ferreira, H.; Bidoia, E.D. Antibacterial action and target mechanisms of zinc oxide nanoparticles against bacterial pathogens. *Sci. Rep.* **2022**, *12*, 2658. [[CrossRef](#)]
38. Mirhosseini, F.; Amiri, M.; Daneshkazemi, A.; Zandi, H.; Javadi, Z.S. Antimicrobial Effect of Different Sizes of Nano Zinc Oxide on Oral Microorganisms. *Front. Dent.* **2019**, *16*, 105. [[CrossRef](#)]
39. Zanet, V.; Vidic, J.; Auger, S.; Vizzini, P.; Lippe, G.; Iacumin, L.; Comi, G.; Manzano, M. Activity evaluation of pure and doped zinc oxide nanoparticles against bacterial pathogens and *Saccharomyces cerevisiae*. *J. Appl. Microbiol.* **2019**, *127*, 1391–1402. [[CrossRef](#)] [[PubMed](#)]
40. Tiwari, V.; Mishra, N.; Gadani, K.; Solanki, P.S.; Shah, N.A.; Tiwari, M. Mechanism of anti-bacterial activity of zinc oxide nanoparticle against Carbapenem-Resistant *Acinetobacter baumannii*. *Front. Microbiol.* **2018**, *9*, 1218. [[CrossRef](#)]
41. Mthana, M.S.; Mthiyane, M.N.; Ekennia, A.C.; Singh, M.; Onwudiwe, D.C. Cytotoxicity and antibacterial effects of silver doped zinc oxide nanoparticles prepared using fruit extract of Capsicum Chinense. *Sci. Afr.* **2022**, *17*, e01365. [[CrossRef](#)]
42. Sirelkhatim, A.; Mahmud, S.; Seeni, A.; Kaus, N.H.M.; Ann, L.C.; Bakhori, S.K.M.; Hasan, H.; Mohamad, D. Review on Zinc Oxide Nanoparticles: Antibacterial Activity and Toxicity Mechanism. *Nanomicro Lett.* **2015**, *7*, 219–242. [[CrossRef](#)]
43. Mohd Yusof, H.; Mohamad, R.; Zaidan, U.H.; Abdul Rahman, N.A. Microbial synthesis of zinc oxide nanoparticles and their potential application as an antimicrobial agent and a feed supplement in animal industry: A review. *J. Anim. Sci. Biotechnol.* **2019**, *10*, 57. [[CrossRef](#)]
44. Zhao, L.; Liu, Z.; Chen, D.; Liu, F.; Yang, Z.; Li, X.; Yu, H.; Liu, H.; Zhou, W. Laser Synthesis and Microfabrication of Micro/Nanostructured Materials Toward Energy Conversion and Storage. *Nano-Micro Lett.* **2021**, *13*, 49. [[CrossRef](#)]
45. Palneedi, H.; Park, J.H.; Maurya, D.; Peddigari, M.; Hwang, G.T.; Annapureddy, V.; Kim, J.W.; Choi, J.J.; Hahn, B.D.; Priya, S.; et al. Laser Irradiation of Metal Oxide Films and Nanostructures: Applications and Advances. *Adv. Mater.* **2018**, *30*, e1705148. [[CrossRef](#)]
46. Zyoud, S.H.; Ahmed, N.M.; Lahewil, A.S.Z.; Omar, A.F. Micro spot ZnO nanotubes using laser assisted chemical bath deposition: A low-cost approach to UV photodetector fabrication. *Sens. Actuators A Phys.* **2022**, *338*, 113485. [[CrossRef](#)]
47. Mutluay Unal, S.; Ozkir, S.E.; Seyfioglu Polat, Z.; Guven, S.; Asutay, H. The Effect of Ytterbium-Doped Fiber Laser with Different Parameters on Physical Properties of Zirconia Surface. *Photomed. Laser Surg.* **2017**, *35*, 157–163. [[CrossRef](#)]
48. Wang, L.; Wang, Z.; Wang, Z.; Zhang, C.; Wu, Y.; Zheng, H. Enhancement of antibacterial function by incorporation of silver-doped ZnO nanocrystals onto a laser-induced graphene surface. *RSC Adv.* **2021**, *11*, 33883–33889. [[CrossRef](#)]
49. Masa, A.; Jehsoh, N.; Dueramae, S.; Hayeemasae, N. Boosting the Antibacterial Performance of Natural Rubber Latex Foam by Introducing Silver-Doped Zinc Oxide. *Polymers* **2023**, *15*, 1040. [[CrossRef](#)] [[PubMed](#)]
50. Ramesh, A.M.; Pal, K.; Kodandaram, A.; Manjula, B.L.; Ravishankar, D.K.; Gowtham, H.G.; Murali, M.; Rahdar, A.; Kyzas, G.Z. Antioxidant and photocatalytic properties of zinc oxide nanoparticles phyto-fabricated using the aqueous leaf extract of *Sida acuta*. *Green Process. Synth.* **2022**, *11*, 857–867. [[CrossRef](#)]
51. Noman, M.T.; Amor, N.; Petru, M.; Mahmood, A.; Kejzlar, P. Photocatalytic Behaviour of Zinc Oxide Nanostructures on Surface Activation of Polymeric Fibres. *Polymers* **2021**, *13*, 1227. [[CrossRef](#)] [[PubMed](#)]
52. Hannachi, E.; Slimani, Y.; Nawaz, M.; Trabelsi, Z.; Yasin, G.; Bilal, M.; Almessiere, M.A.; Baykal, A.; Thakur, A.; Thakur, P. Synthesis, characterization, and evaluation of the photocatalytic properties of zinc oxide co-doped with lanthanides elements. *J. Phys. Chem. Solids* **2022**, *170*, 110910. [[CrossRef](#)]
53. Wagner, E.; Maudez, W.; Bagdzevicius, S.; Sandu, S.C.; Benvenuti, G. Chemical beam vapour deposition technique with Sybilla equipment: Review of main results in its 20-year anniversary. *Oxide-Based Mater. Devices* **2021**, *11687*, 135–154. [[CrossRef](#)]
54. Pakma, O.; Özyayın, C.; Özden, Ş.; Kariper, I.A.; Güllü, Ö. Synthesis and characterization of vanadium oxide thin films on different substrates. *J. Mater. Sci. Mater. Electron.* **2017**, *28*, 10909–10913. [[CrossRef](#)]
55. Wang, X.; Ahmad, M.; Sun, H. Three-Dimensional ZnO Hierarchical Nanostructures: Solution Phase Synthesis and Applications. *Materials* **2017**, *10*, 1304. [[CrossRef](#)]
56. Chauhan, V.P.; Popović, Z.; Chen, O.; Cui, J.; Fukumura, D.; Bawendi, M.G.; Jain, R.K. Fluorescent nanorods and nanospheres for real-time in vivo probing of nanoparticle shape-dependent tumor penetration. *Angew. Chem. Int. Ed. Engl.* **2011**, *50*, 11417–11420. [[CrossRef](#)] [[PubMed](#)]
57. Handore, K.; Bhavsar, S.; Horne, A.; Chhattise, P.; Mohite, K.; Ambekar, J.; Pande, N.; Chabukswar, V. Novel Green Route of Synthesis of ZnO Nanoparticles by Using Natural Biodegradable Polymer and Its Application as a Catalyst for Oxidation of Aldehydes. *J. Macromol. Sci. Part A* **2014**, *51*, 941–947. [[CrossRef](#)]
58. Li, J.; Guo, J.; Dai, H. Probing dissolved CO₂(aq) in aqueous solutions for CO₂ electroreduction and storage. *Sci. Adv.* **2022**, *8*, 399. [[CrossRef](#)]
59. Sabry, R.S.; Rahmah, M.I.; Aziz, W.J. A systematic study to evaluate effects of stearic acid on superhydrophobicity and photocatalytic properties of Ag-doped ZnO nanostructures. *J. Mater. Sci. Mater. Electron.* **2020**, *31*, 13382–13391. [[CrossRef](#)]
60. Kwon, D.; Kim, J. Silver-doped ZnO for photocatalytic degradation of methylene blue. *Korean J. Chem. Eng.* **2020**, *37*, 1226–1232. [[CrossRef](#)]

61. Mohammadzadeh Kakhki, R.; Tayebee, R.; Ahsani, F. New and highly efficient Ag doped ZnO visible nano photocatalyst for removing of methylene blue. *J. Mater. Sci. Mater. Electron.* **2017**, *28*, 5941–5952. [[CrossRef](#)]
62. Chauhan, A.; Verma, R.; Kumari, S.; Sharma, A.; Shandilya, P.; Li, X.; Batoo, K.M.; Imran, A.; Kulshrestha, S.; Kumar, R. Photocatalytic dye degradation and antimicrobial activities of Pure and Ag-doped ZnO using Cannabis sativa leaf extract. *Sci. Rep.* **2020**, *10*, 7881. [[CrossRef](#)]
63. Zhang, L.; Mohamed, H.H.; Dillert, R.; Bahnemann, D. Kinetics and mechanisms of charge transfer processes in photocatalytic systems: A review. *J. Photochem. Photobiol. C Photochem. Rev.* **2012**, *13*, 263–276. [[CrossRef](#)]
64. Liu, S.; Huang, G.; Wang, J.; Bao, J.; Wang, M.; Wei, Y.; Zhong, Y.; Bai, F. Noble Metal Nanoparticle-Loaded Porphyrin Hexagonal Submicrowires Composites (M-HW): Photocatalytic Synthesis and Enhanced Photocatalytic Activity. *Nanomaterials* **2023**, *13*, 660. [[CrossRef](#)]
65. Ghosh, S.; Goudar, V.S.; Padmalekha, K.G.; Bhat, S.V.; Indi, S.S.; Vasan, H.N. ZnO/Ag nano hybrid: Synthesis, characterization, synergistic antibacterial activity and its mechanism. *RSC Adv.* **2012**, *2*, 930–940. [[CrossRef](#)]
66. Li, F.; Zhang, Q.; Liu, J.; Cui, N.; Guan, G.; Huang, W. Electron promoted ZnO for catalytic synthesis of higher alcohols from syngas. *Green Energy Environ.* **2022**, *7*, 1390–1400. [[CrossRef](#)]
67. Sun, M.; Kong, W.; Zhao, Y.; Liu, X.; Xuan, J.; Liu, Y.; Jia, F.; Yin, G.; Wang, J.; Zhang, J. Improving Photocatalytic Degradation Activity of Organic Pollutant by Sn⁴⁺ Doping of Anatase TiO₂ Hierarchical Nanospheres with Dominant {001} Facets. *Nanomaterials* **2019**, *9*, 1603. [[CrossRef](#)]
68. Wang, M.; Tan, G.; Feng, S.; Yin, L.; Wang, Y.; Zhang, B.; Lv, L.; Ren, H. Construction of Ag/NaBiO₃ with dual active sites for photocatalytic NO deep oxidation and long-lasting organic pollutants degradation in the dark. *J. Hazard. Mater.* **2021**, *416*, 125877. [[CrossRef](#)] [[PubMed](#)]
69. Khan, I.; Saeed, K.; Khan, I. Nanoparticles: Properties, applications and toxicities. *Arab. J. Chem.* **2019**, *12*, 908–931. [[CrossRef](#)]
70. Naskar, A.; Lee, S.; Kim, K.S. Easy One-Pot Low-Temperature Synthesized Ag-ZnO Nanoparticles and Their Activity Against Clinical Isolates of Methicillin-Resistant Staphylococcus aureus. *Front. Bioeng. Biotechnol.* **2020**, *8*, 216. [[CrossRef](#)]
71. Elbasuney, S.; El-Sayyad, G.S.; Tantawy, H.; Hashem, A.H. Promising antimicrobial and antibiofilm activities of reduced graphene oxide-metal oxide (RGO-NiO, RGO-AgO, and RGO-ZnO) nanocomposites. *RSC Adv.* **2021**, *11*, 25961–25975. [[CrossRef](#)] [[PubMed](#)]
72. Khalid, A.; Ahmad, P.; Alharthi, A.I.; Muhammad, S.; Khandaker, M.U.; Faruque, M.R.I.; Din, I.U.; Alotaibi, M.A.; Khan, A. Synergistic effects of Cu-doped ZnO nanoantibiotic against Gram-positive bacterial strains. *PLoS ONE* **2021**, *16*, e0251082. [[CrossRef](#)]
73. Manoharan, C.; Pavithra, G.; Bououdina, M.; Dhanapandian, S.; Dhamodharan, P. Characterization and study of antibacterial activity of spray pyrolysed ZnO:Al thin films. *Appl. Nanosci.* **2016**, *6*, 815–825. [[CrossRef](#)]
74. Kim, J.S.; Kuk, E.; Yu, K.N.; Kim, J.-H.; Park, S.J.; Lee, H.J.; Kim, S.H.; Park, Y.K.; Park, Y.H.; Hwang, C.-Y.; et al. Antimicrobial effects of silver nanoparticles. *Nanomedicine* **2007**, *3*, 95–101. [[CrossRef](#)]
75. SonDI, I.; Salopek-SonDI, B. Silver nanoparticles as antimicrobial agent: A case study on, E. coli as a model for Gram-negative bacteria. *J. Colloid Interface Sci.* **2004**, *275*, 177–182. [[CrossRef](#)]
76. Dimapilis, E.A.S.; Hsu, C.S.; Mendoza, R.M.O.; Lu, M.C. Zinc oxide nanoparticles for water disinfection. *Sustain. Environ. Res.* **2018**, *28*, 47–56. [[CrossRef](#)]
77. Rai, M.; Yadav, A.; Gade, A. Silver nanoparticles as a new generation of antimicrobials. *Biotechnol. Adv.* **2009**, *27*, 76–83. [[CrossRef](#)] [[PubMed](#)]
78. Feng, Q.L.; Wu, J.; Chen, G.Q.; Cui, F.Z.; Kim, T.N.; Kim, J.O. A mechanistic study of the antibacterial effect of silver ions on Escherichia coli and Staphylococcus aureus. *J. Biomed. Mater. Res.* **2000**, *52*, 662–668. [[CrossRef](#)] [[PubMed](#)]
79. Patel, J.B.; Eliopoulos, G.M.; Jenkins, S.G.; James Lewis, F.S., II; Brandi Limbago, P.; Nicolau, D.P.; Robin Patel, F.; Powell, M.; Sandra Richter, F.S.; Jana Swenson, D.M.; et al. *Performance Standards for Antimicrobial Susceptibility Testing Performance Standards for Antimicrobial Susceptibility Testing Suggested Citation*, 29th ed.; Clinical & Laboratory Standards Institute: Wayne, PA, USA, 2019; Volume 39, ISBN 9781684400324.

Disclaimer/Publisher's Note: The statements, opinions and data contained in all publications are solely those of the individual author(s) and contributor(s) and not of MDPI and/or the editor(s). MDPI and/or the editor(s) disclaim responsibility for any injury to people or property resulting from any ideas, methods, instructions or products referred to in the content.